



HAL
open science

Airborne lidar measurements of XCO₂ in synoptically active environment and associated comparisons with numerical simulations

Samantha Walley, Sandip Pal, Joel Campbell, Jeremy Dobler, Emily Bell, Brad Weir, Sha Feng, Thomas Lauvaux, David Baker, Nathan Blume, et al.

► To cite this version:

Samantha Walley, Sandip Pal, Joel Campbell, Jeremy Dobler, Emily Bell, et al.. Airborne lidar measurements of XCO₂ in synoptically active environment and associated comparisons with numerical simulations. *Journal of Geophysical Research: Atmospheres*, 2022, 127 (16), 10.1029/2021jd035664 . hal-03762642

HAL Id: hal-03762642

<https://hal.science/hal-03762642v1>

Submitted on 28 Aug 2022

HAL is a multi-disciplinary open access archive for the deposit and dissemination of scientific research documents, whether they are published or not. The documents may come from teaching and research institutions in France or abroad, or from public or private research centers.

L'archive ouverte pluridisciplinaire **HAL**, est destinée au dépôt et à la diffusion de documents scientifiques de niveau recherche, publiés ou non, émanant des établissements d'enseignement et de recherche français ou étrangers, des laboratoires publics ou privés.



Distributed under a Creative Commons Attribution 4.0 International License



RESEARCH ARTICLE

10.1029/2021JD035664

Special Section:

Carbon Weather: Toward the next generation of regional greenhouse gas inversion systems

Key Points:

- First airborne observations of column average CO₂ dry-air mole-fraction (XCO₂) changes across fronts observed during ACT-A are reported
- XCO₂ frontal structures compare reasonably well with Weather Research and Forecasting—Chemistry and an in situ data driven assimilation system
- Results reveal that the differences across models and data were generally much smaller than the magnitude of XCO₂ frontal contrasts

Supporting Information:

Supporting Information may be found in the online version of this article.

Correspondence to:

S. Pal,
Sandip.pal@ttu.edu

Citation:

Walley, S., Pal, S., Campbell, J. F., Dobler, J., Bell, E., Weir, B., et al. (2022). Airborne lidar measurements of XCO₂ in synoptically active environment and associated comparisons with numerical simulations. *Journal of Geophysical Research: Atmospheres*, 127, e2021JD035664. <https://doi.org/10.1029/2021JD035664>

Received 4 AUG 2021

Accepted 7 AUG 2022

Author Contributions:

Conceptualization: Sandip Pal, Kenneth J. Davis

Data curation: Sandip Pal, Joel F. Campbell, Jeremy Dobler, Brad Weir, Sha Feng, Thomas Lauvaux, Nathan Blume,

© 2022. The Authors.

This is an open access article under the terms of the [Creative Commons Attribution License](#), which permits use, distribution and reproduction in any medium, provided the original work is properly cited.

Airborne Lidar Measurements of XCO₂ in Synoptically Active Environment and Associated Comparisons With Numerical Simulations

Samantha Walley¹ , Sandip Pal¹ , Joel F. Campbell² , Jeremy Dobler³ , Emily Bell⁴, Brad Weir^{5,6} , Sha Feng^{7,8} , Thomas Lauvaux^{8,9}, David Baker⁴, Nathan Blume³, Wayne Erxleben¹⁰, Tai-Fang Fan¹¹ , Bing Lin², Doug McGregor³, Michael D. Obland², Chris O'Dell⁴ , and Kenneth J. Davis^{7,12} 

¹Department of Geosciences, Atmospheric Science Division, Texas Tech University, Lubbock, TX, USA, ²NASA Langley Research Center (LaRC), Hampton, VA, USA, ³Spectral Sensor Solutions LLC, Fort Wayne, IN, USA, ⁴Colorado State University, Fort Collins, CO, USA, ⁵Universities Space Research Association, Columbia, MD, USA, ⁶NASA Goddard Space Flight Center, Greenbelt, MD, USA, ⁷Atmospheric Sciences and Global Change Division, Pacific Northwest National Laboratory, Richland, WA, USA, ⁸Department of Meteorology and Atmospheric Science, The Pennsylvania State University, University Park, PA, USA, ⁹LSCE - IPSL, CEA Saclay, Saclay, France, ¹⁰L3 Harris Technologies, Melbourne, FL, USA, ¹¹Science System and Application, Inc, Hampton, VA, USA, ¹²Earth and Environmental Systems Institute, The Pennsylvania State University, University Park, PA, USA

Abstract Frontal boundaries have been shown to cause large changes in CO₂ mole-fractions, but clouds and the complex vertical structure of fronts make these gradients difficult to observe. It remains unclear how the column average CO₂ dry air mole-fraction (XCO₂) changes spatially across fronts, and how well airborne lidar observations, data assimilation systems, and numerical models without assimilation capture XCO₂ frontal contrasts (Δ XCO₂, i.e., warm minus cold sector average of XCO₂). We demonstrated the potential of airborne Multifunctional Fiber Laser Lidar (MFL) measurements in heterogeneous weather conditions (i.e., frontal environment) to investigate the Δ XCO₂ during four seasonal field campaigns of the Atmospheric Carbon and Transport-America (ACT-America) mission. Most frontal cases in summer (winter) reveal higher (lower) XCO₂ in the warm (cold) sector than in the cold (warm) sector. During the transitional seasons (spring and fall), no clear signal in Δ XCO₂ was observed. Intercomparison among the MFL, assimilated fields from NASA's Global Modeling and Assimilation Office (GMAO), and simulations from the Weather Research and Forecasting—Chemistry (WRF-Chem) showed that (a) all products had a similar sign of Δ XCO₂ though with different levels of agreement in Δ XCO₂ magnitudes among seasons; (b) Δ XCO₂ in summer decreases with altitude; and (c) significant challenges remain in observing and simulating XCO₂ frontal contrasts. A linear regression analyses between Δ XCO₂ for MFL versus GMAO, and MFL versus WRF-Chem for summer-2016 cases yielded a correlation coefficient of 0.95 and 0.88, respectively. The reported Δ XCO₂ variability among four seasons provide guidance to the spatial structures of XCO₂ transport errors in models and satellite measurements of XCO₂ in synoptically-active weather systems.

1. Introduction

Greenhouse gases play an essential role in governing Earth's radiation budget while atmospheric CO₂ has been rising at an increasing rate (e.g., 1.50 ppm/year for 1990–1999, 1.97 ppm/year for 2000–2009, 2.40 ppm/year for 2010–2019; Peters et al., 2020). Very recently, the daily average of atmospheric CO₂ concentrations at Mauna Loa observatory in Hawaii was recorded as high as 421.21 ppm (NOAA-GML). Human activities, such as burning fossil fuels and deforestation, disturb the natural balance between CO₂ sources and sinks and are causing this increase (Salam & Noguchi, 2005; Schneider et al., 2021), making quantification of CO₂ sources and sinks essential to long term climate monitoring (Barnes et al., 2016; Masarie et al., 2014). Terrestrial ecosystem carbon fluxes are particularly uncertain, and earth system models differ vastly in their simulations of projected terrestrial CO₂ uptake in a rapidly changing climate (e.g., Keenan & Williams, 2018).

An improved understanding of the spatiotemporal changes in atmospheric CO₂ due to weather systems will strengthen our ability to infer uptake and release of CO₂ from terrestrial ecosystems and the ocean through inverse methods. High-resolution observations of CO₂ vertical and spatial variability across different spatial scales (e.g.,

Wayne Erxleben, Tai-Fang Fan, Bing Lin, Doug McGregor, Michael D. Obland

Formal analysis: Samantha Walley, Sandip Pal, Joel F. Campbell, Jeremy Dobler, Nathan Blume, Wayne Erxleben, Doug McGregor

Funding acquisition: Sandip Pal

Investigation: Samantha Walley, Sandip Pal, Kenneth J. Davis

Methodology: Samantha Walley, Sandip Pal, Joel F. Campbell, Jeremy Dobler, Emily Bell, Thomas Lauvaux, David Baker, Tai-Fang Fan, Bing Lin, Michael D. Obland, Chris O'Dell

Project Administration: Sandip Pal

Resources: Sandip Pal, Michael D. Obland

Software: Samantha Walley, Joel F. Campbell, Jeremy Dobler, Emily Bell, Brad Weir, Sha Feng, Nathan Blume, Wayne Erxleben, Bing Lin, Doug McGregor, Michael D. Obland

Supervision: Sandip Pal

Validation: Samantha Walley, Joel F. Campbell, Jeremy Dobler, Emily Bell, Brad Weir, Sha Feng, Thomas Lauvaux, Tai-Fang Fan, Bing Lin, Doug McGregor, Chris O'Dell

Visualization: Samantha Walley

Writing – original draft: Samantha Walley

Writing – review & editing: Sandip Pal, Joel F. Campbell, Jeremy Dobler, Emily Bell, Brad Weir, Sha Feng, Thomas Lauvaux, David Baker, Nathan Blume, Wayne Erxleben, Bing Lin, Michael D. Obland, Chris O'Dell, Kenneth J. Davis

local, synoptic, global) help resolve estimates of surface fluxes at global and regional scales (e.g., Chevallier et al., 2010). Barnes et al. (2016) attributed the recent changes in northern high latitude seasonal cycle CO₂ amplitude to changes in midlatitude surface fluxes but lacked observations of isentropic transport of CO₂ across latitudes. Schuh et al. (2019) reported that large-scale transport uncertainty resulted in a 1.7 PgC/year bias present in the inverse estimation in both high latitude bands (45°N–90°N and 45°S–90°S).

As air masses transport over different ecosystems, the CO₂ spatial variability is primarily affected by underlying fluxes (Lan et al., 2017; Sweeney et al., 2015) and atmospheric boundary layer (ABL) features (Lee et al., 2015, 2018; Pal et al., 2017). The impact of synoptic air mass transport on CO₂ vertical and horizontal distributions remained unclear as annual average vertical variability was presented without consideration of air mass differences (Sweeney et al., 2015). Synoptic-scale processes modulate fluxes via cloud-radiation feedback (Chan et al., 2004), and precipitation-soil moisture–atmosphere feedback (Humphrey et al., 2021). However, a significant gap remains in our understanding of the impact of synoptic-scale weather systems and associated vertical exchanges due to convection on CO₂ transport.

Previously, Hurwitz et al. (2004) and Lee et al. (2012) used NOAA's tall tower measurements to investigate the effects of frontal passages on the CO₂ variability in the lower-most part of the ABL, noted rapid changes in ABL-CO₂, and speculated about the presence of large CO₂ gradients in the troposphere. Using airborne in situ measurements, Pal, Davis, Lauvaux, et al. (2020) showed how the CO₂ distributions in the ABL, and free troposphere (FT) vary spatially across individual frontal systems during summer and also reported the presence of an enhanced band of CO₂ in the ABL in the vicinity of frontal boundaries. However, it remained unclear how CO₂ distributions in the entire lower troposphere change in presence of synoptic scale events (e.g., frontal passage, squall lines).

High-resolution (e.g., 1 km spatially) airborne lidar measurements of XCO₂ across frontal boundaries would illustrate the CO₂ spatial variability in the entire lower troposphere and can potentially complement in situ CO₂ observations, and aid in satellite validation (e.g., Campbell et al., 2020). Bell et al. (2020) provided examples of the accuracy and ability of the Orbiting Carbon Observatory - 2 (OCO-2) to observe XCO₂ spatial variability in fair weather via comparison with both in situ data assimilated into a curtain by an atmospheric model and observations from the airborne Multifunctional Fiber Laser Lidar (MFLL).

Satellite measurements provide a valuable tool for analyzing global CO₂ measurements. However, because OCO-2 makes passive measurements and depends on reflected sunlight, clouds inhibit this process, yielding high uncertainties in the measurements obtained in cloudy regimes (O'Dell et al., 2018). The Total Carbon Column Observing Network (TCCON) provides temporal variability of XCO₂ with respect to a synoptic scale weather passage (Wunch et al., 2011); however, TCCON measurements also contain gaps and can become erroneous in presence of clouds. Additionally, due to the sparse network, the horizontal XCO₂ spatial variability remains unresolved (Chevallier et al., 2011; O'Dell et al., 2012). On the other hand, OCO-2 derived fields of XCO₂ are also not adequate to obtain samples across frontal boundaries due to excessive cloudiness often present near frontal boundaries (Bell et al., 2020; O'Dell et al., 2018; Wunch et al., 2017).

High spatially resolved information of XCO₂ variability in the presence of synoptic-scale weather patterns are available from the airborne lidar observations collected during the Atmospheric Carbon and Transport—America (ACT-America) field campaigns (Davis et al., 2021; Pal & Davis, 2021). The primary benefit of the airborne lidar measurements over satellite or TCCON measurements are the lidar's potential to obtain measurements through thin or scattered clouds, and the fact that the aircraft often flew below high clouds. Aircraft measurements sampled XCO₂ variability across frontal boundaries and provide adequate measurements in warm and cold sectors within a brief time (~1 hr; Bell et al., 2020; Campbell et al., 2020).

The key aims of this work are to investigate (a) the impact of mid-latitude cyclones on XCO₂ spatial variability, in particular, XCO₂ frontal contrasts (i.e., ΔXCO_2), over the eastern US in four seasons; (b) how well the global and mesoscale transport model simulations capture ΔXCO_2 ; and (c) how model-data mismatches (MDMs) vary between frontal and fair weather conditions. These investigations help obtain the typical spatial distribution of XCO₂ variability in the atmosphere during frontal passages (Figure 1). Since for the first time, we collected systematic MFLL measurements across frontal boundaries from different altitudes, it remains beneficial to demonstrate the potential of MFLL measurements in heterogeneous water vapor environment (i.e., warm moist sector vs. dry cold sector), typically involved during the passage of mid-latitude cyclones. We also explored

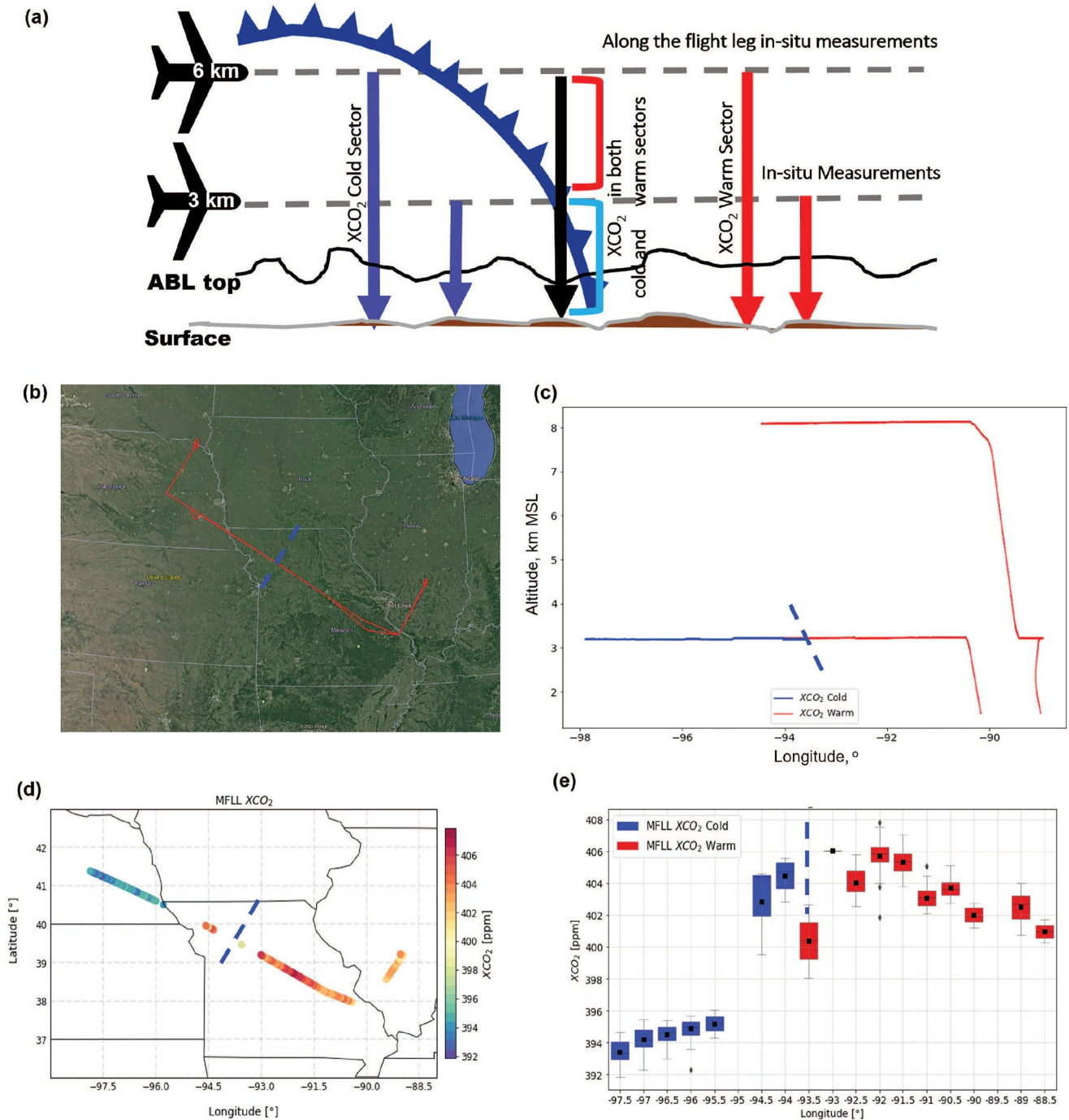


Figure 1. Schematic of a frontal research flight (RF) showing multifunctional fiber laser lidar (MFL) measurements onboard C-130 from two altitudes (3 and 6 km MSL) sampling XCO₂ in both the warm (red arrows) and cold (blue arrows) sectors of the front. The region near the frontal boundary (slanted navy curve with triangles) indicates XCO₂ measurements referring to both warm and cold sector columns in vertical. In situ measurements of CO₂ were also performed along those legs. Black and gray curved lines mark the atmospheric boundary Layer (ABL) top and surface, respectively (a); C-130 track (red line overlaid on the map) during the RF on 12 August 2016 (b); Longitude-versus-altitude view of the frontal flags used to indicate warm (red) and cold (blue) sectors along C-130 tracks (c); XCO₂ (3 km MSL column) spatial variability across the front (d); 0.5° longitude segmented box and whisker plot across the frontal boundary where the blue and red boxes represent XCO₂ in the cold and warm sector, respectively (e); The black square and horizontal line inside the boxes indicate the mean and median, respectively. The end of the bars represents points that lie within 1.5 interquartile ranges, with the black diamonds representing values that fall outside of that range. The dashed blue line on each panel marks the frontal boundary.

XCO₂ retrieved by WRF-Chem simulations, that is not optimized by ACT-America measurements but is fed NOAA CarbonTracker fluxes and boundary conditions (Peters et al., 2007; with updates documented at <https://carbontracker.noaa.gov>). Finally, we also used XCO₂ variability estimated using a different transport model that is optimized using ACT-America in situ measurements from NASA's GMAO to investigate Δ XCO₂.

The remaining parts of the paper are organized as follows. Sections 2 introduces the datasets, instruments and model simulation used while Section 3 presents the details of the methodology to estimate XCO₂ frontal contrasts, enhancement, and MDMs in all the relevant metrics where we provided an example case to illustrate the MDM framework. Results pertaining to observed XCO₂ frontal contrasts, MDMs, and frontal enhancement are reported in Section 4. Followed by an extended discussion in Section 5, and brief conclusions and outlook are finally provided in Section 6.

2. Data Set, Instruments, and Models

2.1. ACT-America

Within the ACT-America project, five field campaigns were carried out (summer-2016, winter-2017, fall-2017, spring-2018, and summer-2019) over three eastern US regions: Mid-Atlantic (MA), Midwest (MW), and South (SO) (Davis et al., 2021); during the summer-2019 campaign, the MFL was not deployed. During most research flights (RFs), two aircraft were flown (B-200 and C-130) to obtain reactive trace gases (CO, O₃), greenhouse gases (CO₂, CH₄) and meteorological measurements during fair weather and frontal weather conditions (Davis et al., 2018; Pal & Davis, 2021; Wei et al., 2021). The C-130 aircraft flew at several different altitudes, often in the upper and lower FT, and acquired MFL measurements of XCO₂ (Lin et al., 2020). The B-200, housing a suite of similar in situ instruments, flew in the ABL and mid FT, typically collocated along a portion of the C-130 ground tracks so that both CO₂ and XCO₂ observations along with the meteorological measurements are collected along similar flight paths across the fronts.

During the first four campaigns, 38 frontal RFs were conducted, but some of the high-altitude flights (e.g., 4.5, 5.5 and 8 km MSL) were eliminated for this study due to the lack of XCO₂ measurements for extensive cloud cover beneath the MFL platform at the lower altitudes, mostly in the warm sector of the frontal systems (e.g., see Figure 1c for frontal flags along 8 km MSL altitude during a RF on 12 Aug 2016). All the frontal RFs available through ACT-America are described in Table S1 (see Supporting Information S1). One should note that the C-130 flight altitudes varied for the selected cases (2.5–8 km MSL, Table S1 in Supporting Information S1). To achieve the goals of this work, we required XCO₂ samples in both warm and cold sectors to investigate XCO₂ frontal contrasts. Many high-altitude flights sampled only one of the two frontal sectors. Additionally, some frontal RFs were made in such a way that MFL observations were not useful due to the changing altitudes of the MFL platform (C-130). Though it is possible to obtain XCO₂ for the altitudes between cloud top and MFL platform (i.e., partial columns without the entire depth of the atmosphere from MFL platform to ground), we did not consider those measurements to be appropriate to fulfill our research goals. Previously, Lin et al. (2020) discussed the flagging and retrieval of XCO₂ in those partial columns. To the best of the authors' knowledge, there exist no systematic XCO₂ measurements across frontal boundaries in the literature.

Finally, 27 cases were selected for the investigation of the XCO₂ frontal contrasts (henceforth, Δ XCO₂). The ideal C-130 flight pattern for frontal RFs included 2 level flight legs of C-130 across a frontal boundary, varying in altitude from lower to upper free troposphere (Figure 1a) which illustrates that quantification of Δ XCO₂ using MFL-XCO₂ measurements remains complicated by the slanted shape of the frontal boundary. Thus, we considered the XCO₂ measurements far from the frontal boundary to compute warm and cold sector averages of XCO₂ to estimate the Δ XCO₂ and analyzed the XCO₂ measurements near the vicinity of frontal boundary separately to understand the front relative XCO₂ features (an enhancement in XCO₂ spatial structures, see Section 3.3).

2.2. Multifunctional Fiber Laser Lidar (MFL)

The MFL was developed by Harris Corp. and NASA Langley Research Center (Dobler et al., 2013). The MFL uses the Integrated Path Differential Absorption (IPDA) technique to measure the differential absorption optical depth (DOAD) of the online and offline wavelengths at the CO₂ absorption line centered at 1,571.112 nm (Campbell et al., 2020). Optical depths from the MFL data and meteorological variables from the Modern-Era

Retrospective analysis for Research and Applications, Version 2 (MERRA-2; Gelaro et al., 2017) reanalysis data were then used to retrieve XCO₂ (Campbell et al., 2020). Additional details on the XCO₂ retrieval, its spectroscopic model, etc. are available elsewhere (e.g., Bell et al., 2020; Campbell et al., 2020; Gordon et al., 2017) while MFLN weighting function and Lite files are available in Lin et al. (2022a, 2022b).

During the XCO₂ retrievals, a number of calibration and corrections were applied including (a) filtering lidar signals collected for more than 5° pitch/roll angles, (b) cloud-screening via discriminating the signals between ground and intermediate scatterers (i.e., clouds) using the matched filter technique, (c) altitude dependent bias correction using CO₂ profiles obtained at cloud-free conditions and modeled XCO₂ values obtained using in situ measurements of meteorological parameters and CO₂ concentrations (Campbell et al., 2020). The MFLN-XCO₂ measurements were found to have a signal-to-noise ratio (SNR) of 120, 330, 950 and 1,600 for averaging times of 0.1, 1, 10 and 60 s, corresponding to a precision of 3.4, 1.2, 0.43, and 0.26 ppm, respectively. The XCO₂ measurement precision was estimated by the standard deviation of the measured XCO₂ samples with the stated averaging (i.e., 0.1, 1, 10, and 60 s) under spatially homogeneous conditions while the SNR was estimated via calculating mean XCO₂ divided by the standard deviation of XCO₂ during certain flight length.

The results pertaining to the measurement precision and SNR were obtained via dedicated MFLN flights over the Gulf of Mexico under relatively homogeneous conditions in presence of onshore flow. For instance, the mean CO₂ concentrations (using in situ measurements on C-130 aircraft) along two different ABL legs across a distance of more than 200 km over water were found to be 405.15 and 405.17 ppm while the corresponding standard deviations were 0.09 and 0.08 ppm, respectively. Additionally, on a one-hour time scale, the average drift was below 0.1 ppm. Campbell et al. (2020) provided some comprehensive details on calibration measurement performance of MFLN under different atmospheric conditions.

2.3. The GMAO Curtain

NASA's GMAO produces fields of XCO₂ through the assimilation of in situ CO₂ measurements collected using both the C-130 and B-200 aircraft, referred to here as curtains (Bell et al., 2020). The GMAO product has 72 vertical levels from the surface to 0.01 hPa with a 0.5° by 0.625° spatial resolution is output every 3 hr and recently has been used as part of the calibration and validation of MFLN retrievals at 8 km (Campbell et al., 2020). The GMAO product is used here as a proxy for in situ data as it fills in data where it is missing using modeled correlations. It uses fluxes calibrated to in situ data (Weir et al., 2021) that are similar to the input fluxes used by WRF-Chem. Using a similar approach introduced in Bell et al. (2020), we used XCO₂ retrieved from the GMAO assimilated curtains (henceforth, GMAO-XCO₂) to explore Δ XCO₂.

2.4. The WRF-Chem Model

The Weather Research and Forecasting—Chemistry (WRF-Chem) model derived XCO₂ field was compared to the MFLN observations to evaluate the XCO₂ variability in this modeling system (Feng, Lauvaux, Davis, et al., 2019; Skamarock et al., 2008). The CO₂ fluxes included in WRF-Chem were obtained from NOAA Carbon-Tracker (CT) v2017 for summer-2016 and Near Real Time v2019-2 (CT-NRT.v 2019-2) for the other three campaigns beyond 2016. CO₂ was included as a passive tracer in WRF-Chem (Lauvaux et al., 2012). In general, CT assimilates observations at the rate of each measurement (from hourly to weekly depending on types of available observations) and at resolution of eco-regions for land and large ocean regions, and weekly scaling factors for each flux regions. CT outputs are available at 3-hourly temporal resolution at 1° × 1° spatial resolution and provides the carbon surface fluxes from the terrestrial biosphere, oceans, fossil fuels, wildfires, and atmospheric CO₂ mole fractions (Jacobson et al., 2007, 2020). Additional details on the WRF-Chem model setup and performance can be found elsewhere (Feng, Lauvaux, Keller, et al., 2019; Gerken et al., 2021; Samaddar et al., 2021).

WRF-Chem was run at 27-km covering most of North America from 1 June 2016 to 30 June 2019. In the entire simulation period, the meteorology was driven with ERA5 and run 5 days including a 12-hr spin-up; the first month is considered the CO₂ spin up, and CO₂ is carried over in each meteorological cold start. At the end, we concatenated the 4.5 days simulation in each simulation window, and all the analyses used here are based on them.

2.5. Computing XCO₂ for Comparison to MFL

Following Bell et al. (2020), simulated XCO₂ was trimmed down and interpolated to match the MFL observations along the C-130 tracks during all the RFs so that XCO₂ field from both WRF-Chem (henceforth, WRF-XCO₂) and GMAO were available at a spatial resolution of 1,100 m corresponding to each XCO₂ sample collected using MFL at a temporal resolution of 10 s (i.e., equivalent to horizontal distance of 1,100 m with an average C-130 aircraft speed of 110 m s⁻¹). For intercomparison of XCO₂ fields, we did not use GMAO-XCO₂ and WRF-XCO₂ when or where MFL had data gaps to keep a similar number of XCO₂ samples in simulation and observations.

The MFL uses a pressure weighting function (PWF) which favors CO₂ concentrations at higher altitudes in the observed column and which can affect the observed XCO₂ in non-negligible ways when compared to a “straight” pressure-weighted calculation (Bell et al., 2020). The MFL PWF was derived for each individual sounding along a flight track; we used the coincident MFL PWFs to calculate XCO₂ from the resampled GMAO and WRF-Chem CO₂ fields, ensuring that the vertical sensitivity is consistent between MFL observations and model estimates. Following Bell et al. (2020), we sampled GMAO in situ “curtain” column up to the C-130 height to produce a partial-column value which uses a straight pressure weighting function.

3. Methods

3.1. Quality Control of MFL-XCO₂ Measurements

The MFL-XCO₂ had many anomalous data points not filtered by the correction approach outlined in Section 2.2. To remove the additional outliers, we developed a standard deviation filter method to eliminate these anomalous data points (Figure S1 in Supporting Information S1). Each case was analyzed individually to identify the appropriate standard deviation to be applied for the filter. The standard deviation filter was applied to both 10 s averaged and 1 s measurements of XCO₂. The XCO₂ differences between the filtered data at 1s and the averaged data with a filter taken at 10 s were analyzed, and the only samples with XCO₂ differences between the two samples that were within ±1 ppm of XCO₂ were kept for further analyses.

Before we applied the standard-deviation based filter approach to remove outliers in XCO₂ samples, we made an extensive amount of sensitivity tests for XCO₂ measurements collected during both fair weather and frontal crossing RFs. Those tests were performed separately for each case and appropriate filter value was chosen. We applied the filters simultaneously in two stages, namely for 1 and 10-s averaged XCO₂ values. When the results of both averaged-sets identified identical outliers (i.e., spike), we removed them for the remainder of the analyses. The histogram analyses for all the samples also yielded those identified samples (i.e., outliers) to be located far from the distributions as expected due to the application of the standard deviation approach. Being a conservative approach based on sensitivity tests for individual cases, we finally eliminated less than 0.01% of samples from the entire flight leg for each case, though it varied among the cases as evinced in the example results presented in Figure S1 in Supporting Information S1. Thus, we note the filtering technique did not change the frontal contrast results. In the past, a very similar standard-deviation based approach (often called histogram analyses) was used in other lidar-based studies to remove spikes from lidar measurements (e.g., Pal et al., 2010; Senff et al., 1994; Turner et al., 2014; Wulfmeyer et al., 2010).

This technique allowed for removing the outliers in all the cases, as illustrated in the example case of an MW flight on 30 October 2017 (Figure S1 in Supporting Information S1). The XCO₂ (2.2 km MSL column) variability in a longitudinal plane across a cold front is presented with a direct comparison between the different filtered data and unfiltered data averaged to 10 s. As depicted by the yellow crosses, the anomalous data points are filtered out using the approach described above. In further analyses, we used only the measurements represented by the black stars. The spikes in the XCO₂ field are most likely caused by low SNR in the presence of clouds.

However, we identified four frontal RFs (11 October 2017; 7 March 2017; 16 May 2018; 20 August 2016, Table S1 in Supporting Information S1) during which MFL-XCO₂ measurements were extraordinarily erroneous even after the application of the different corrections, calibration and the standard deviation filter. The MFL overall accuracy for these cases was of lower quality most likely due to very high water vapor variability in the atmosphere that was not well represented in the reanalysis product used for retrieving XCO₂. Consequently, we decided to eliminate the XCO₂ measurements for those RFs for further analyses and for overall MDM explorations.

3.2. XCO₂ Frontal Contrasts

The frontal boundary along the individual flight legs was determined based on the in situ measurements of thermodynamic variables, particularly temperature and dew point temperature, as described in Pal, Davis, Lauvaux, et al. (2020). As illustrated in Figure 1 (panels b, c, d, and e), in the vicinity of the frontal boundary (longitude of 93.5°W), the MFLC samples warm and cold sectors due to the natural slope or baroclinic feature of the frontal boundary. To avoid this region's inclusion in the XCO₂ frontal contrast calculation, the flight track was divided into half-degree segments of latitude or longitude on either side of the frontal boundary as indicated by the frontal flags. The frontal contrast (i.e., ΔXCO₂) was calculated using

$$\Delta XCO_2 = \overline{XCO_2^{\text{Warm}}} - \overline{XCO_2^{\text{Cold}}}$$

where $\overline{XCO_2^{\text{Warm}}}$ and $\overline{XCO_2^{\text{Cold}}}$ represent the average XCO₂ in the furthest half-degree segments of latitude or longitude depending on the frontal orientation along the flight track in the warm and cold sectors, respectively. Such selection far away from the frontal boundary provided the advantage that we were able to avoid selecting partial columns with mixture of warm and cold sector air mass (in vertical direction) in the vicinity of frontal boundaries (Figure 1a). For instance, if the C-130 flight legs were oriented along the north to south plane crossing the frontal boundary orthogonally, we considered the farthest 0.5° latitude sectors in the north and south for cold and warm sectors, respectively. Thus, for the analyses of ΔXCO₂ for all the RFs, we were able to exclude the XCO₂ samples obtained in the “enhanced XCO₂” region. Additionally, the lengths of the C-130 flight legs in the warm and cold sector varied, with more sampling typically in the warm sector than in the cold sector for majority of the RFs. A similar approach was applied to calculate ΔXCO₂ for both GMAO-XCO₂ and WRF-XCO₂.

To illustrate the methodology for determining ΔXCO₂, we presented MFLC-XCO₂ measurements obtained on 4 August 2016 over the MW region during the summer-2016 field campaign (Figure 2). During this flight, the C-130 flew a distance of 810 km across a frontal boundary located in central Missouri such that it was possible to obtain enough XCO₂ samples in both warm and cold sectors. The MFLC measurements from an altitude of 5.5 km MSL suggested significant XCO₂ spatial variability with higher XCO₂ in the warm sector than in the cold sector. The frontal flags obtained along 5.5 km MSL leg clearly indicate the frontal boundary at the location of 94°W which was used as a reference for estimating XCO₂. The box and whisker analyses depict the average XCO₂ at a resolution of 0.5°-longitude segments (i.e., ~50 km horizontal resolution, Figure 2h). The furthest average XCO₂ (0.5°-longitude segment) in the cold sector at −97.5° was subtracted from the furthest average XCO₂ (0.5°-longitude segment) in the warm sector at −93.5°. From this, a XCO₂ of 2.1 ppm was found. Additionally, we found a very similar pattern in the spatial variability in ABL-CO₂ field and MFLC measured XCO₂ field on this day although the sampling domains in longitudes were slightly different (Figures 2d and 2h).

3.3. XCO₂ Enhancement Near the Frontal Boundary

Previously, while investigating frontal contrasts in CO₂ concentrations in both ABL and FT for summer-2016 field campaign, Pal, Davis, Lauvaux, et al. (2020) found a region of enhanced CO₂ in the ABL in the vicinity of frontal boundaries. Using the MFLC measurements of the XCO₂ field, a very similar feature was noted in some cases (Tables S1 and S2 in Supporting Information S1). For each case, the XCO₂ enhancement feature was further investigated by analyzing the XCO₂ average values in the enhanced region compared to the warm sector's average-XCO₂. The width of the enhanced XCO₂ band was estimated by analyzing the mean XCO₂ in the half-degree longitude or latitude segments that were elevated near the frontal boundary compared to the warm-sector average XCO₂. The XCO₂ enhancement was calculated by subtracting average warm sector XCO₂ from the enhanced region's average XCO₂.

3.4. Model Data Comparison

An intercomparison among the MFLC-XCO₂, GMAO-XCO₂, and WRF-XCO₂ was conducted to investigate the XCO₂ spatial variability across frontal boundaries obtained via MFLC observations and two model fields. WRF-Chem has not been optimized using the in situ airborne observations while GMAO-simulations were used to create curtains using the ACT-America in situ CO₂ mole fraction observations. Two types of comparisons were

4 Aug 2016

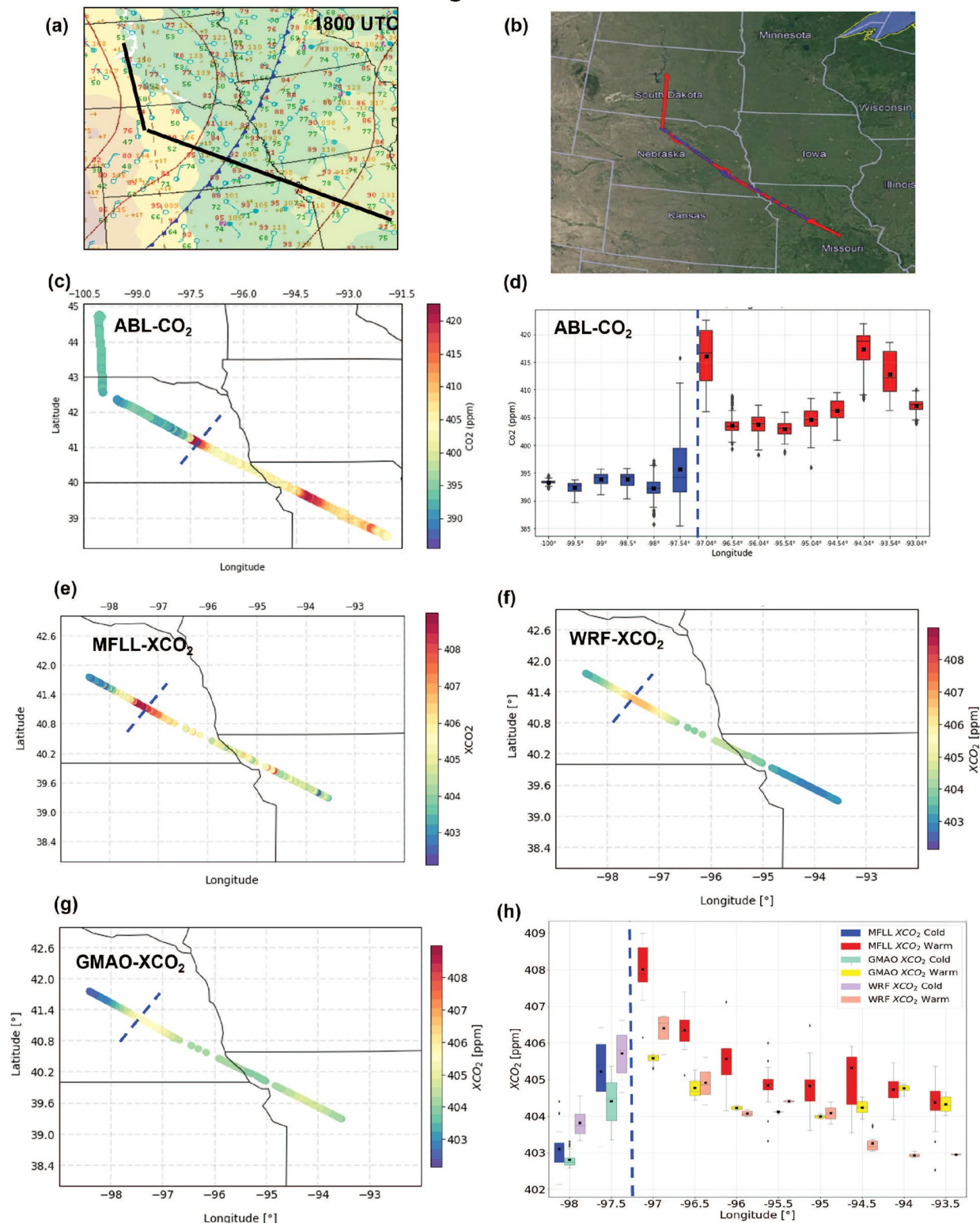


Figure 2.

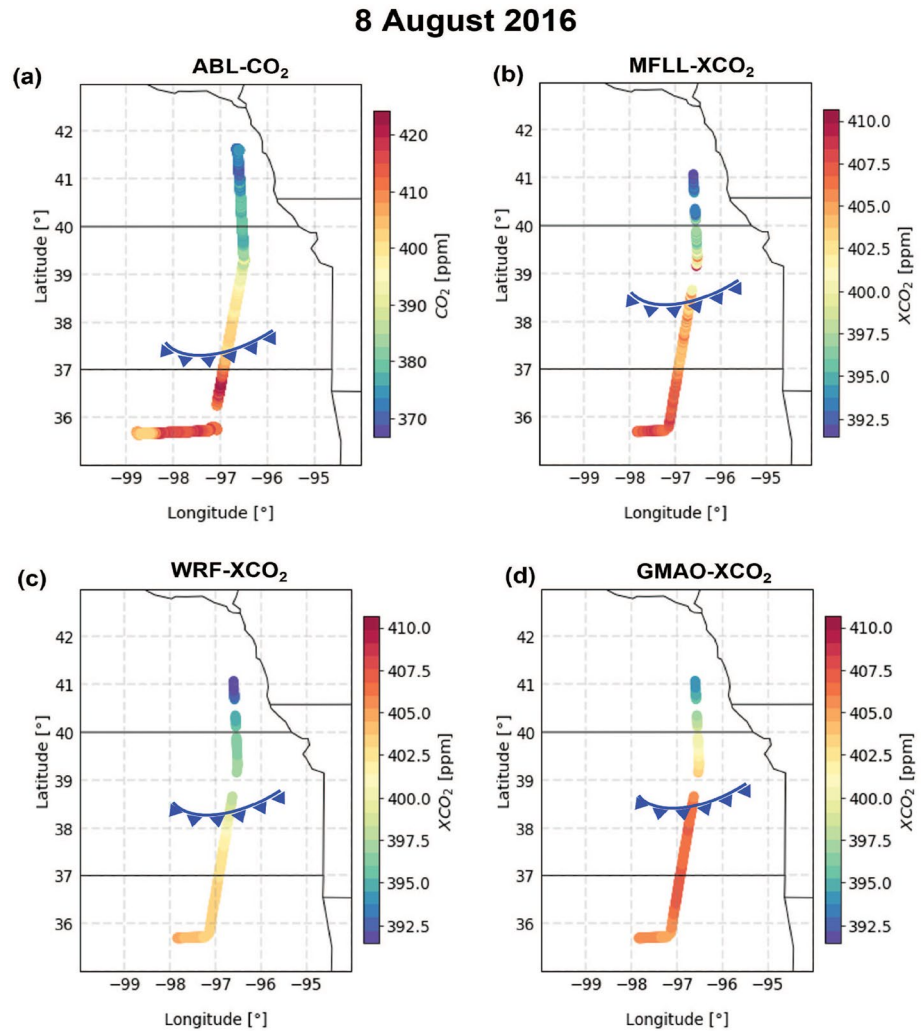


Figure 3. A multi-parameter view of frontal crossing research flight on 8 August 2016 showing in situ measurements of CO_2 mole fractions yielding ABL- CO_2 spatial variability (a), XCO_2 derived using multifunctional fiber laser lidar (MFL) on board C-130 along the north-south transect (b), WRF-Chem simulation (c), and Global Modeling and Assimilation Office (GMAO) assimilated curtains (d). The MFL XCO_2 spatial variability across the frontal boundary at 3.5 km MSL was obtained after 0.5 hr of B-200 sampled ABL- CO_2 along the same track. Note that the color bar scale limits for panel a (i.e., in situ CO_2 measurements) differs from the other panels (XCO_2 measurements). Location of frontal boundary on each panel is marked by a curved blue line with triangles.

conducted: a comparison of the ΔXCO_2 and a comparison of the average XCO_2 sampled in both warm and cold sectors.

Figure 3 shows the two different types of measurements (in situ measurements of ABL- CO_2 and MFL- XCO_2), GMAO- XCO_2 , and WRF- XCO_2 for an example frontal RF on 8 Aug 2016. This MW flight spanned across eastern Oklahoma, Kansas, and Nebraska, and the MFL data was collected at around 3.5 km MSL. A cold front was located near the Oklahoma/Kansas border as shown on the ABL- CO_2 field (see frontal boundary in ABL at $\sim 37.3^\circ\text{N}$ in Figure 3a). The MFL measurements along the same track also shows very similar front-relative features in XCO_2 (Figure 3b) as was observed for the ABL- CO_2 field confirming higher values in both XCO_2

Figure 2. Model data comparison for an example frontal research flight (RF) in summer (4 August 2016, Figure 4) along with the flight tracks shown on a surface map (a) and on Google map; red: C-130 and blue: B-200 (b). ABL- CO_2 spatial variability (c); XCO_2 (5.5 km MSL column) retrieved using MFL (e), WRF-Chem (f) and GMAO (g). The box and whisker plots for both ABL- CO_2 (d) and XCO_2 from three products binned into 0.5° longitude segments with XCO_2 from the MFL XCO_2 in the warm (red) and cold (blue) sectors, WRF-Chem in the warm (pink) and cold (purple) sectors, and GMAO in the warm (yellow) and cold (aqua) sectors. Blue dashed-line on each panel marks the frontal boundary.

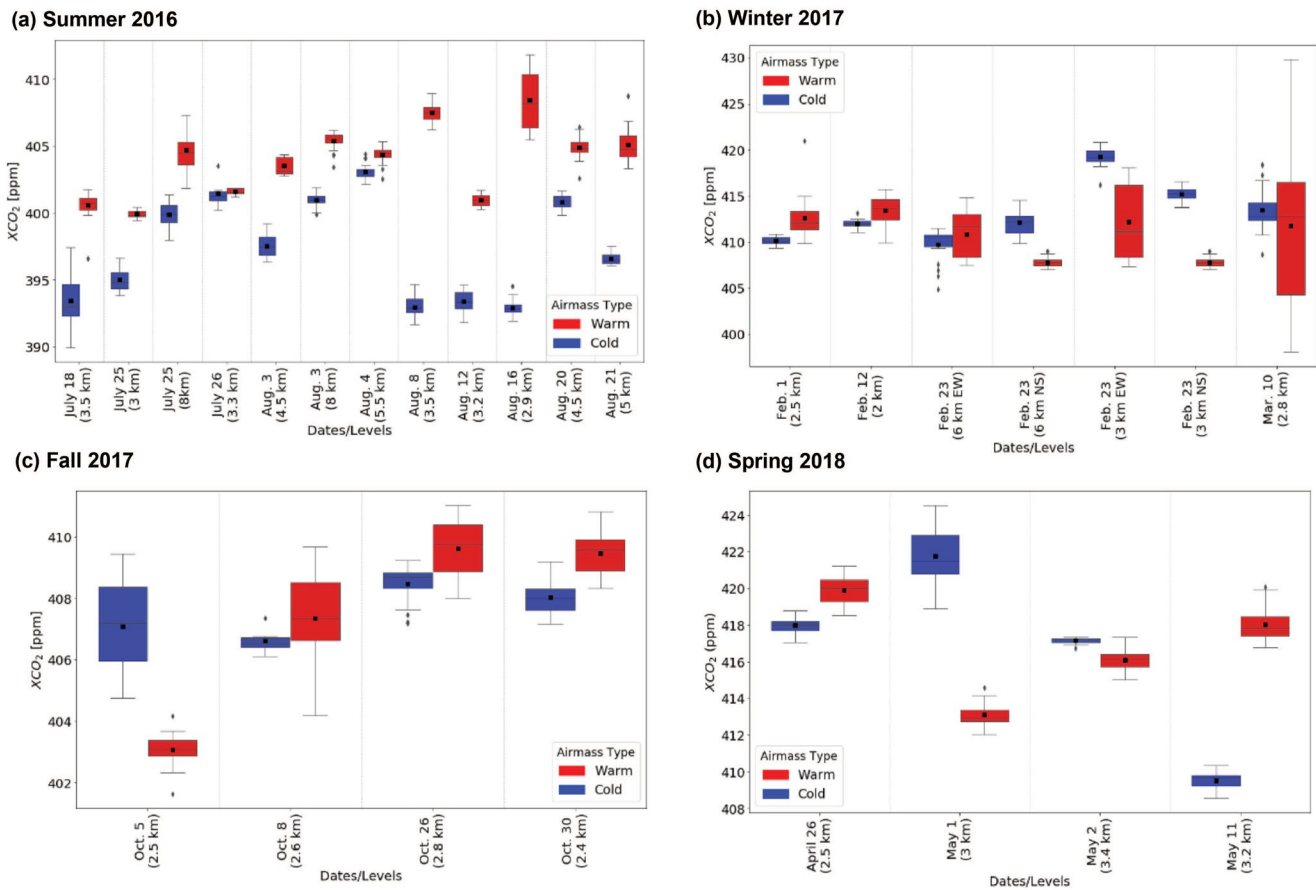


Figure 4. Seasonal summary of XCO₂ variability in both warm and cold sectors of the frontal systems during the RFs of summer-2016 (a), winter-2017 (b), fall-2017 (c), and spring-2018 (d). Each red and blue pair of boxes corresponds to XCO₂ in the furthest 0.5° region of warm and cold sectors of the flight path, respectively. The box and whisker plots here and in other figures are represented in the same manner as Figure 1e.

and CO₂ in the warm sector than the cold sector. The frontal boundary along the 3.5 km MSL flight leg (located ~38.5°N) is also marked illustrating the frontal slope illustrated in Figure 1a. It can be seen that the overall XCO₂ spatial variability observed by MFL was captured well by both GMAO and WRF-Chem (see Supporting Information S1 for similar analyses for all the frontal RFs). For brevity, a single case for the three other seasons is briefly described in Supporting Information (see Supporting Information S1) to exemplify the model data intercomparison framework.

4. Results

4.1. XCO₂ Frontal Contrasts in Four Seasons

Based on the method discussed in Section 3.2, a comprehensive summary of the XCO₂ variability in the warm and cold sectors for all frontal RFs (Table S1 in Supporting Information S1) is first presented via box and whisker analyses (Figure 4). We note overview figures for all the frontal RFs (Table S1 in Supporting Information S1) during four field campaigns (summer-2016: Figures S6–S18; winter 2017: Figures S19–S24; fall 2017: Figures S25–S28; and spring 2018: Figures S29–S31) are presented in Supporting Information S1. Also included is a box and whisker diagram that divides the flight track into 0.5° latitude or longitude boxes and depicts the airmass type across the front. As reported in Supporting Information S1 (Table S1 and Figures S3–S31 in Supporting Information S1), the C-130 altitudes (i.e., the MFL platform) varied among different altitudes within a RF and among the RFs since the frontal RFs were designed in such a way that both remote sensing measurements of XCO₂ and in situ measurements of CO₂ were available in both warm and cold sectors in three different altitudes (e.g., ABL, lower free troposphere and upper free troposphere) over a wide region (400–800 km) while fulfilling

the other aims of the RF missions of ACT-America campaigns (e.g., the MFLC calibration, obtaining profiles of thermodynamic variables and GHGs and trace gases via en-route ascent, descent, and targeted spirals).

However, while reporting XCO_2 frontal contrasts, we compared the findings for the similar altitudes. Table S1 also provides some comprehensive information on each of the frontal crossing RFs including dates, regions, average flight altitudes for each level (red indicated the cases chosen for this work) including the rationale for the choice of the cases, weather conditions in the region of the flight, frontal flags, and comments if there was a region of enhanced XCO_2 (where green represents the cases chosen for further XCO_2 enhancement investigation), and finally, the reasoning for our choice of XCO_2 enhancement cases.

These results (Figure 4 and Table S1 in Supporting Information S1) help explore the XCO_2 spatial variability across frontal boundaries among different RFs in four seasons. One should note that the MFLC altitudes varied among the RFs, as shown in the x -axis of Figure 4, so that case-to-case variability of XCO_2 structures in both the warm and cold sectors should be interpreted with caution, as multiple altitudes are considered. As seen in Figure 4a, out of the 10 days, for a total of 12 cases, the average ΔXCO_2 for summer was 8.5 ppm for 3-km altitude flights, the largest average ΔXCO_2 across all the seasons. The representative warm sector 0.5° mean of XCO_2 was always higher than that of the cold sector. In winter (see Figure 4b), there were a total of 7 cases, with several being the same day, just at different levels or sampling regions (Table S1 in Supporting Information S1). The average ΔXCO_2 for 3-km MSL MFLC observations in the winter was -7.4 ppm. In five of the seven cases, the warm sector XCO_2 was less than that of the cold sector XCO_2 , while the rest of the cases mimicked summer findings.

The measurements of fall-2017 and spring-2018 provide a complex view into what happens to XCO_2 during these transition seasons (Figures 4c and 4d). As broad latitudinal regions were sampled, different growth stages or dormancy in the plants depending on the region were observed. In the fall (see Figure 4c), all but 5 October 2017, out of the four MW and MA cases mimic the summer structure. The average ΔXCO_2 for 2.8 km MSL altitude for fall-2017 is 1.8 ppm. Again, this follows a pattern like summer but with a lesser ΔXCO_2 magnitude. In spring-2018, two out of the four in the MW and MA had higher values of XCO_2 in the warm sector than in the cold sector. The average ΔXCO_2 for spring-2018 was 2.2 ppm. Thus, during these transition seasons (fall and spring), we did not find any clear signal in ΔXCO_2 . In general, there exist a spatial variability (south to north) in phenology in both fall and spring over the broad regions of the eastern US (Liu et al., 2021). For instance, the most productive regions are located in the north (Hilton et al., 2017; Miles et al., 2012). During the ACT-America field campaigns, due to the fairly long north-south transects (~ 600 km) of the RFs. We indeed found phenology to be more variable in those two seasons. Thus, it is plausible that one portion of the frontal RF was more over a “spring like” atmosphere where plants are growing versus some areas that might have still been in dormancy leading to a more “winter like” atmosphere. Nevertheless, more analyses are required to determine the contribution of spatial variability of phenology to ΔXCO_2 , if any.

4.2. XCO_2 Enhancements Near Fronts

A region of enhanced XCO_2 near the frontal boundary was noted in several cases (Table S2 in Supporting Information S1). An example case illustrating the regions of ABL- CO_2 and XCO_2 enhancements along flight track on 4 August 2016 is presented in Figure 2 (panels c and e). During this MW RF, aircraft transected a cold front in southwestern Nebraska at around 1800 UTC. A thin band of clouds was present in the region of the frontal boundary, with light precipitation. Results clearly indicate that both ABL- CO_2 and MFLC- XCO_2 were higher in the warm sector than the cold sector with varying degrees of ΔCO_2 and ΔXCO_2 due to the differences in their nature of sampling (in situ sampling within ABL only vs. columnar measurements of XCO_2). The corresponding box-and-whisker analyses for both parameters are shown in Figures 2d and 2h. The XCO_2 spatial variability in the warm sector also evinced an increasing trend from $94.5^\circ W$ to $97^\circ W$ toward the frontal boundary which we defined as an XCO_2 enhancement and also confirms higher XCO_2 spatial variability in the warm sector than the cold sector. Similar analyses were performed for all the frontal RFs which helped identify an enhancement in the MFLC- XCO_2 (Tables S1 and S2 in Supporting Information S1).

To explore the XCO_2 enhancement feature, the region of enhancement was investigated using two metrics: the width of the XCO_2 enhancement in the direction perpendicular to the front, and the magnitude of the XCO_2 enhancement relative to the average XCO_2 observed in the warm sector. Another example case (20 August 2016)

was chosen to illustrate the XCO₂ enhancement near the frontal boundary in the presence of an extensive cloud cover (Figure S2 in Supporting Information S1) and a summary of all the cases when such features were observed is presented in Table S2 in Supporting Information S1. A region of relatively higher XCO₂ was noted in the vicinity of the front, whose location is identified using the Weather Prediction Center (WPC, 2022) surface analysis. The region of enhanced XCO₂ extends between 33°N and 36.7°N (i.e., a horizontal distance of more than 300 km, marked by an oval shaped curve) along the flight track. The setup of the XCO₂ enhancement along the track at 33°N was determined based on the box-and-whisker analyses when XCO₂ value along the flight track in warm sector was at least 0.5 ppm higher than previous 0.5° box.

We also found that the warm sector XCO₂ decreases gradually after the 36.7°N box (i.e., away from the front). When the XCO₂ in this enhanced region was compared with the warm sector mean XCO₂, the XCO₂ enhancement was found to be around 2.7 ppm. One should note that frontal boundaries are often associated with the presence of optically thick clouds (e.g., Houze et al., 1981; Koch et al., 1995; Pal, Davis, Lauvaux, et al., 2020) yielding data gaps for airborne lidar measurements from an altitude above the clouds; the MFLL measurements during the frontal RFs of ACT-America field campaigns were not an exception to this. Since this is the first time systematic MFLL measurements across frontal boundaries were performed, we were not aware of any algorithm to retrieve and fill the data gaps via interpolation in the XCO₂ field. Consequently, we found it rather important to report the observed variability with data gaps. However, for all the analyses related to XCO₂ enhancement presented here, we confirmed that a sufficient number of XCO₂ samples (i.e., at least two box-and-whisker points) were available. Indeed, a large number of cases when sufficient number of XCO₂ samples were not available to estimate XCO₂ enhancement were excluded, although we observed XCO₂ frontal contrasts in those cases (see Tables S1 and S2 in Supporting Information S1).

Thus, the estimated XCO₂ enhancements reported here do suffer to some extent due to the missing observations in the regions of optically thick clouds along the track beneath the C-130 platform. For a comprehensive description of the flagging method for the presence of clouds, readers are referred to Campbell et al. (2020). The average estimated width of the region of higher XCO₂ is more than 300 km. We acknowledge that these measurement gaps will have an impact on the width and enhancement magnitude results presented. However, currently, we do not have enough quantitative information for an appropriate gap filling procedure and interpolation technique to obtain XCO₂ at those locations.

Our analysis showed considerable case-to-case variability in the magnitude and extent of enhanced XCO₂ features among the cases in addition to the cross-frontal variability in XCO₂ (Table S2 in Supporting Information S1). A common feature noted in all the cases was the presence of clouds at or near the flight. In all but two cases, precipitation was noted near the flight path. One should note that there were some frontal RF cases where we did not observe a clear signature of frontal enhancement, while for some other cases there exists some indication of enhancement in the vicinity of frontal boundaries, but we did not have an appropriate amount of XCO₂ measurements in the warm sector to quantify the XCO₂ enhancement features near the frontal boundary (see, Table S1 in Supporting Information S1). Thus, those were not reported in Table S2 in Supporting Information S1. Nevertheless, we believe that results pertaining to the unprecedented observations of both Δ XCO₂ and the XCO₂ enhancement features reported here will be valuable for both XCO₂ remote sensing and modeling communities to resolve the issues related to “real” signal versus “noise” in XCO₂ measurements in frontal environment.

4.3. Overall Model-Data Intercomparison

To better understand our ability, using models and observations for obtaining a consistent description of the impact of frontal passages on the XCO₂ field, we investigated the three different estimates of Δ XCO₂ (i.e., obtained via MFLL, GMAO, and WRF-Chem) for all cases (Figure 5). There exists a tremendous amount of variability in the observed XCO₂ frontal contrasts potentially due to (a) CO₂ seasonal variability pertaining to the underlying fluxes associated with sources and sinks; (b) diverse nature of frontal passages and associated transport processes in both warm and cold sectors in four seasons; (c) XCO₂ variability among different altitudes; (d) differences in regional scale CO₂ fluxes within a region and among the three ACT-America regions; (e) differences in meteorological characteristics associated with the frontal passages yielding myriad types of optically thick clouds, in particular, in the warm sectors within a RF and among the RFs.

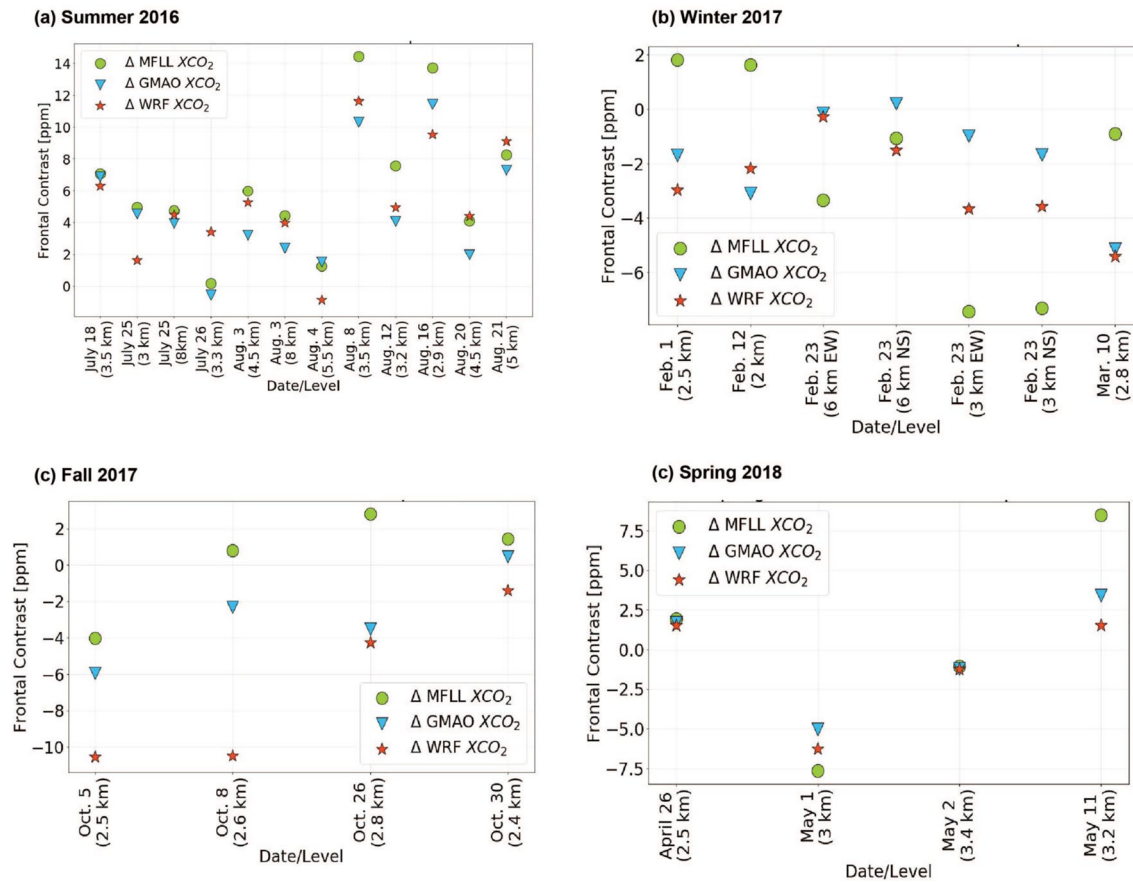


Figure 5. Summary of frontal contrast for each day calculated from the observed multifunctional fiber laser lidar (MFL) XCO₂ (green circles), and modeled XCO₂ from the WRF-Chem (red stars) and Global Modeling and Assimilation Office (GMAO) (blue triangles) for summer-2016 (a), winter-2017 (b), fall-2017 (c), and spring-2018 (d).

During summer-2016, all three products of ΔXCO_2 show similar sign (positive) though with varying magnitudes. However, clearly visible is that the case-to-case variability in ΔXCO_2 was very similar in all three products. In particular, WRF-XCO₂ in summer yielded similar ΔXCO_2 values as MFL (though not identical) for the majority of the cases so that one could state that WRF-Chem simulations reproduced the XCO₂ frontal structures reasonably well and were able to “get the front right” without any ACT-America observations except for a couple of instances. Additionally, ΔXCO_2 variability among the cases in different seasons showed very similar tendency, except WRF-Chem in fall-2017. For instance, the linear regression analyses between ΔXCO_2 obtained from MFL versus GMAO, and MFL versus WRF-Chem for summer-2016 cases yielded a correlation coefficient of 0.95 and 0.88, respectively (Figure 6a). Similar results for the other three seasons are presented in Figure 6b and Table S3 in Supporting Information S1.

Future work investigating the differences in XCO₂ fields via assimilation versus no-assimilation of ACT-America data in the GMAO will help demonstrate the “value” in assimilating ACT-America data. Similarly, exploring the impact of different transport on XCO₂ field via comparing MFL to CT will be another potential research topic but is beyond the scope of this work. We note that, recently, Weir et al. (2021) while illustrating the techniques for bias-corrected surface fluxes derived from satellite observations and Peiro et al. (2022) while using ensembles of multiple atmospheric inversions characterized by different transport models, data assimilation algorithms, and prior fluxes, clearly found that the background for the curtain was of similar skill to CarbonTracker in reproducing independent evaluation data.

Additionally, as the signs of biological fluxes change across seasons, the ΔXCO_2 variability also changed signs (Figure 5). For instance, during winter-2017, all three products showed negative ΔXCO_2 (i.e., lower XCO₂ in the warm sector than the cold sector) except for the MFL-derived ΔXCO_2 for first two cases. To investigate if there

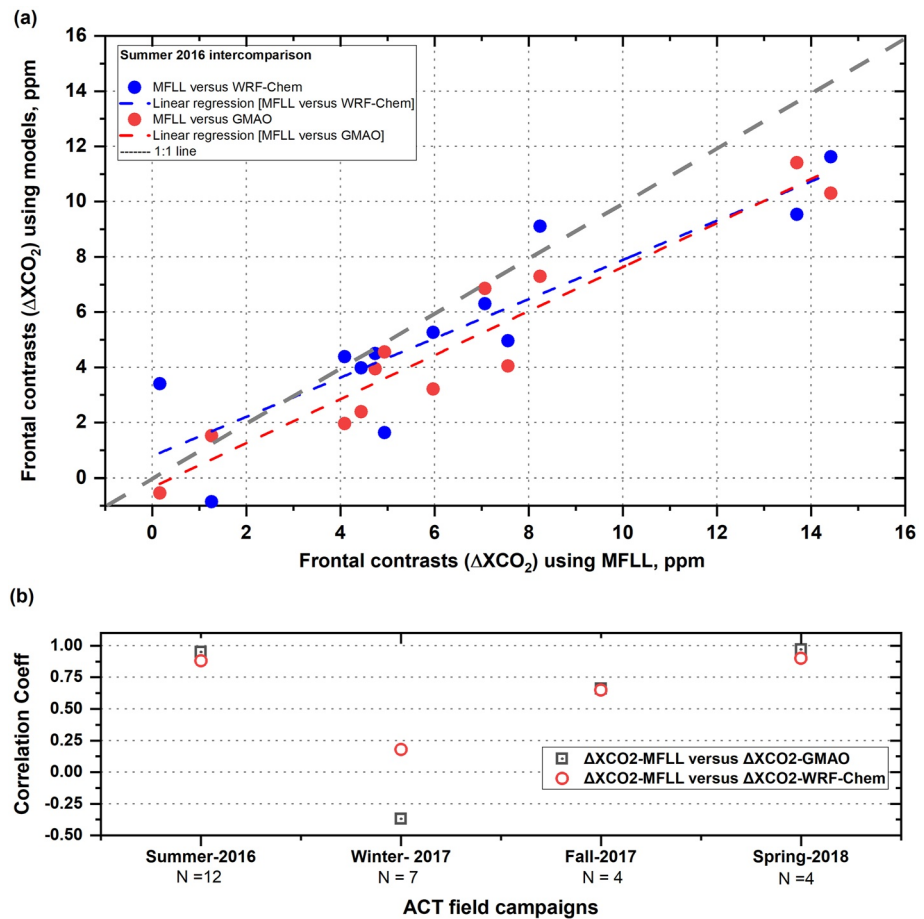


Figure 6. Linear regression analyses between ΔXCO_2 obtained from multifunctional fiber laser lidar (MFL) versus WRF-Chem (blue solid circles and dotted line) and between MFL versus Global Modeling and Assimilation Office (GMAO) (red solid circles and dotted line). Gray dotted line marks the 1:1 line (a). Correlation coefficients obtained from similar linear regression analyses between ΔXCO_2 from MFL and GMAO (gray squares) and between ΔXCO_2 from MFL and WRF-Chem (red circles) for all four ACT-America field campaigns. Number of frontal legs (N) are also indicated for each campaign along the x-axis (b).

exist any seasonal biases among the three products, we explored seasonal means of ΔXCO_2 obtained from MFL, GMAO and WRF-Chem (see Table S4 in Supporting Information S1). Clearly seen is that the ΔXCO_2 values from all three products are similar with respect to magnitude and sign except WRF-Chem in fall-2017 when WRF- ΔXCO_2 was found to be much lower (-6.7 ppm) than both MFL (0.3) and GMAO (-2.8). We note that winter-2017 for MFL is an outlier most likely due to the degradation of the telescope window coating. Correlation coefficients for both ΔXCO_2 comparisons for winter-2017 campaign (MFL vs. GMAO and MFL vs. WRF-Chem) were found to be very low (0.2) and negative (-0.4), respectively (Figure 6b). Nevertheless, these results illustrate how challenging it is to observe and simulate these frontal differences in presence of significant case-to-case XCO_2 variability within and among the seasons.

We also explored the MDM for XCO_2 variability in both warm and cold sectors. For this purpose, the warm and cold sector XCO_2 values for each of the three products were averaged, and then the averages were compared across products (Figure 7). During summer, for MFL versus GMAO, average MDM for warm and cold sectors were -0.6 and 1.3 ppm, respectively while for MFL versus WRF-Chem average differences for warm and cold sectors were -1.0 and 0.7 ppm, respectively. Understanding how these differences compared to that of the cases in fair weather situations would allow for the identification of biases present in the models' ability to replicate XCO_2 spatial variability in frontal environments.

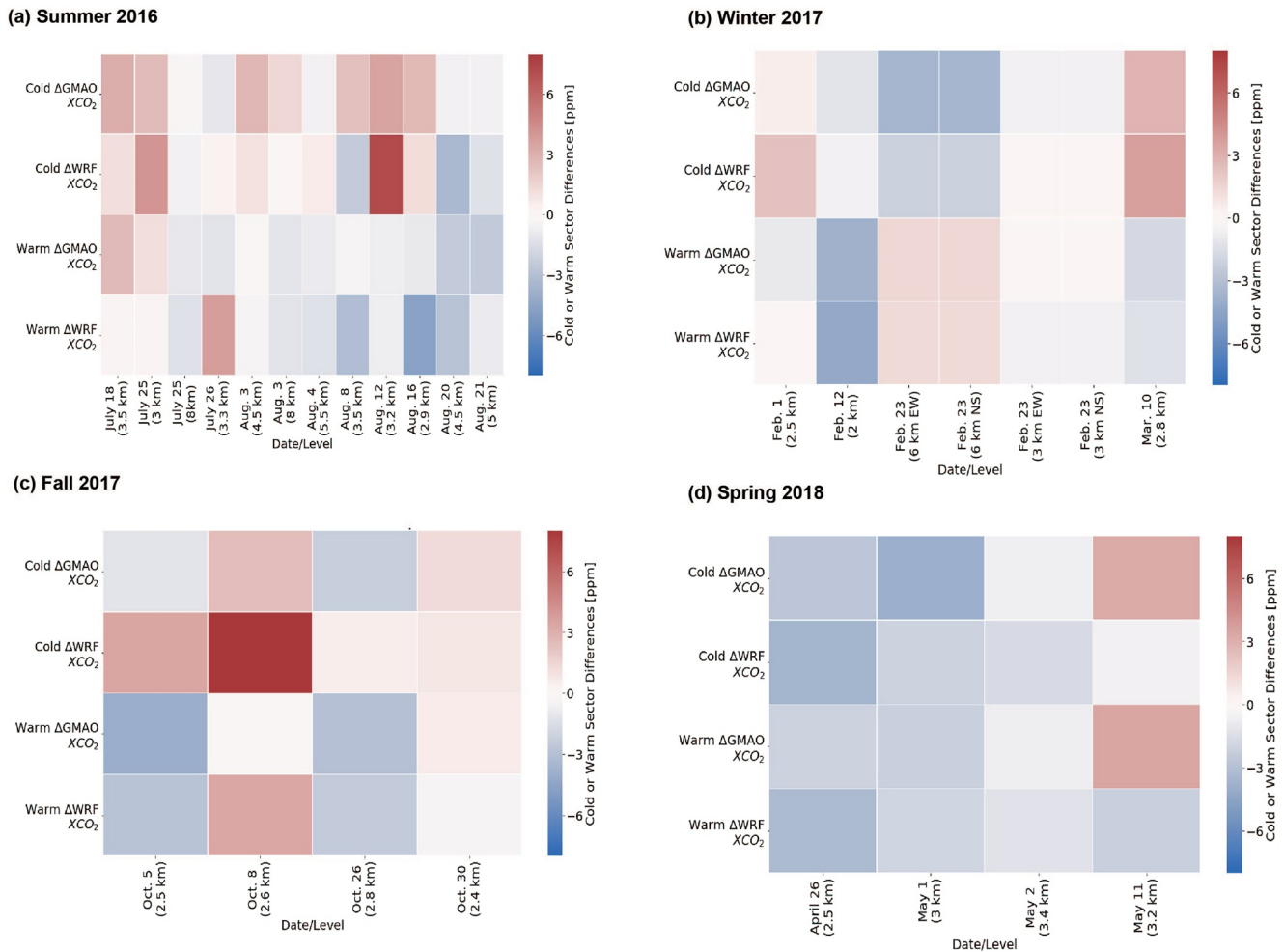


Figure 7. Summary of comparisons between multifunctional fiber laser lidar (MFL) XCO₂ with WRF-Chem and GMAO XCO₂ in both warm and cold sectors for summer-2016 (a), winter-2017 (b), fall-2017 (c), and spring-2018 (d). The red and blue colors represent positive and negative MDM, respectively. The lighter the colors, the smaller is the differences between in XCO₂.

Overall, we found broad similarities in XCO₂ frontal contrast results obtained from MFL, GMAO and WRF-Chem though their degree of agreements varied among the cases and seasons. Previously, using ground-based XCO₂ measurements at TCCON site (Park Falls, Wisconsin), Keppel-Aleks et al. (2012) found that XCO₂ variability even at one location were primarily driven by combined impact of regional-scale fluxes and atmospheric dynamics and also attributed the large-scale gradients of XCO₂ to synoptic-scale meteorological processes. Using airborne in situ measurements of CO₂ fields obtained during the ACT-America RFs, Gerken et al. (2021) exploited the performance of both mesoscale (WRF-Chem) and global scale (CT) models using identical surface fluxes and found reasonable agreement with observations in all four seasons. Additionally, for frontal RFs, Zhang et al. (2022) also found that OCO-2 MIP models were capable of simulating observed CO₂ frontal contrasts with varying degrees of success in summer and spring, and frequent underestimation of frontal contrasts in winter and autumn.

A straightforward conclusion cannot be made here regarding the potential of these models since the models were very different in those studies. In the context of MFL measurements of XCO₂ frontal contrasts and associated intercomparisons, several frontal RFs showed that three XCO₂ products agree reasonably well in all seasons, in particular, potentially marks a great success of mesoscale models (here WRF-Chem) which did not ingest any CO₂ measurements. Nevertheless, we strongly believe that the reported MDMs could be cumulatively attributed to model resolution, assimilated data (for GMAO) and fluxes. One needs to perform more dedicated controlled

experiments to understand the underlying processes and causes driving the differences which is beyond the scope of this work, but certainly remains an important future research topic.

4.4. Intercomparison Between MFLL and GMAO for Fair Weather Cases

To obtain a better understanding on the MDMs in XCO₂, we performed an intercomparison analysis between the MFLL-XCO₂ and GMAO-XCO₂ for some selected fair weather RFs. Recently, Bell et al. (2020) also performed similar comparison but only for OCO-2 underflight cases that were characterized with clear (<20% cloud coverage) and calm wind atmospheric conditions. One should note that within a series of recent ACT-America research work, WRF-Chem simulations were used to compare with aircraft observations for both fair weather and frontal RFs (e.g., Feng, Lauvaux, Davis, et al., 2019; Samaddar et al., 2021). Additionally, Bell et al. (2020) performed a comprehensive intercomparison between XCO₂ fields obtained via MFLL and GMAO for extremely clear sky conditions (OCO-2 underpass flights) and did not use WRF-Chem simulations. Inclusion of additional results based on WRF-Chem would definitely require many additional science questions to be addressed which remained the outside the scope of the present work. Thus, for brevity, we presented substantial new understanding of the earth's atmosphere using MFLL, WRF-Chem and GMAO for frontal environment.

During a MW fair weather RF on 13 August 2016, the synoptic setup was characterized by post-frontal condition with a relatively calm northerly flow (Figure 8a). The cloud physics lidar measurements also confirmed relatively clear sky conditions in the lower altitudes (Pal & Davis, 2021; Pal, Davis, Pauly, et al., 2020). The RF was designed as a box pattern with horizontal legs that sampled east to west and west to east in the boundary layer, as well as the diagonal legs (3.3 km MSL) across the box that sampled the FT when MFLL measurements were available (Figure 8b). These types of box pattern RFs were conducted during the ACT-America campaigns to estimate CO₂ and CH₄ fluxes (Davis et al., 2021).

Figure 8 evinces that there exists XCO₂ spatial variability though without a region of enhanced XCO₂ as was observed during the frontal RFs. Both MFLL and GMAO retrievals show the presence of a clearly visible west-to-east XCO₂ difference (~4–5 ppm in 3.3 km MSL column with XCO₂ values of 398–400 ppm and 394–395 and in the western and eastern parts of the RF tracks, respectively). The GMAO-XCO₂ and MFLL-XCO₂ along both tracks (N1-S1 and N2-S2) agrees reasonably well except the eastern most portion of the RF where MFLL-XCO₂ were 2 ppm higher than the GMAO-XCO₂. However, overall MDMs along N1-S1 and N2-S2 legs were found to be –1.2 and –0.8 ppm, respectively which are much lower than the MDMs obtained during the frontal RFs over the same region. For instance, for frontal RF on 12 August 2016 over the same region, we obtained MDMs (GMAO vs. MFLL) of more than 3.5 ppm (Figure 7a).

An overview of the MDMs for 3 selected fair weather cases in summer-2016 are shown in Supporting Information S1 (see Table S5 and Figure S18 in Supporting Information S1). By comparing the MFLL-XCO₂ and GMAO-XCO₂, the average difference was found to be ~–0.1 ppm, though with some case-to-case variability. Overall, there remains some moderate XCO₂ spatial variability during fair weather cases, but the differences between the GMAO-XCO₂ and the MFLL-XCO₂ remain much smaller to what was found for the frontal RFs (see, Table S5 and Figure 7a). We also found that XCO₂ spatial variability during frontal cases were higher than during the fair weather cases. Cumulatively, these results suggest that higher XCO₂ spatial variability yielded also higher MDMs in XCO₂ and vice-versa.

5. Discussion

5.1. XCO₂ Frontal Contrasts

The 27 cases examined confirm that the XCO₂ field is substantially affected by frontal passages. Based on all three products, a clear pattern was observed in the summer with higher XCO₂ in the warm sector than in the cold sector. Using in situ measurements in the ABL and FT across frontal boundaries, Pal, Davis, Lauvaux, et al. (2020) also found the identical sign in the frontal contrasts in observed CO₂ spatial variability (i.e., higher CO₂ in the warm sector than the cold sector in both ABL and FT), which supports the assertion that the MFLL can identify these patterns. While segregating the frontal contrast results in summer by altitudes, we found that ΔXCO₂ were in general larger in magnitude for low altitudes than for the higher altitudes. For instance, for

13 Aug 2016

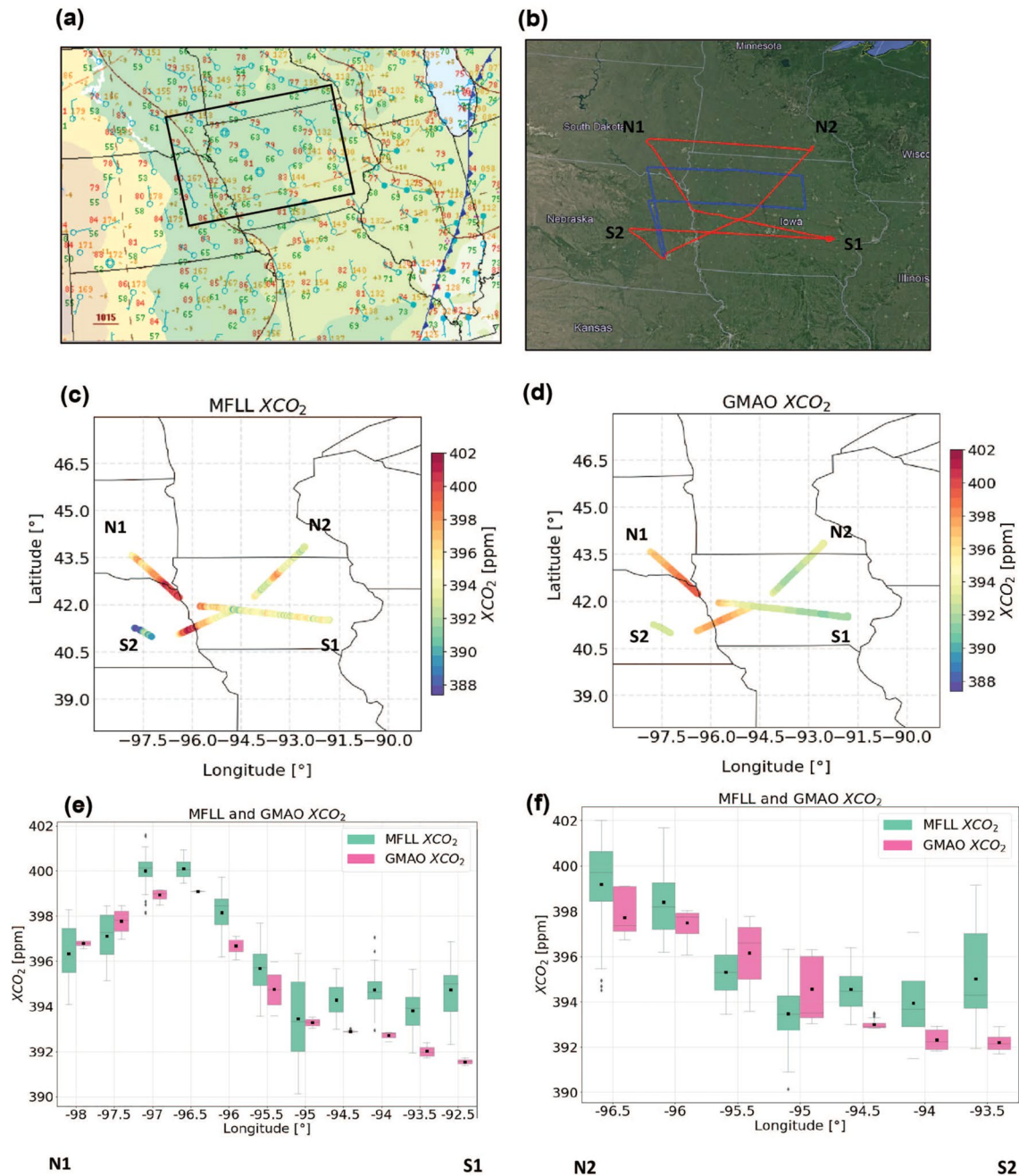


Figure 8. Intercomparison between MFL-XCO₂ and GMAO-XCO₂ fields during a fair weather case in summer (13 August 2016). Surface map illustrating post-frontal fair weather conditions (a) and flight tracks (red: C-130, blue: B-200, panel (b)) showing a typical ACT-America fair weather research flight (here, box pattern under northerly flow as indicated on the surface map). MFL measurements (3.3 km MSL column) along the diagonals (N1-S1 and N2-S2). XCO₂ spatial variability obtained via MFL (c) and GMAO (d) along with the box and whisker plot of the XCO₂ along N1-S1 binned into 0.5° longitude segments for the MFL-XCO₂ (green), and GMAO-XCO₂ (pink) (e); (f) same as (e) but along N2-S2.

summer cases, mean ΔXCO_2 obtained for the altitude ranges of 2.5–3.5, 4.5–3.5, and 8.0 km were 8.0, 4.9 and 4.5 ppm, respectively. One should note that we did not have enough ΔXCO_2 measurements in different altitudes across frontal boundaries in other seasons to determine such altitude dependence feature of ΔXCO_2 , if any (see Table S1 in Supporting Information S1).

The ΔXCO_2 in fall were found to be of similar sign (i.e., positive) as was found for the summer cases except for 5 October 2017. However, the ΔXCO_2 in summer were larger in magnitude compared to fall, most likely due to larger spatial variability in underlying fluxes in summer. One noticeable feature for the 5 October 2017 case was the presence of optically thick clouds in the cold sector unlike the other cases which might have yielded higher XCO_2 in the cold sector than the warm sector yielding contrasting sign in ΔXCO_2 (Figure S4 in Supporting Information S1). These cloud covers most likely yielded reduced photosynthetic uptake as was reported in a number of past studies (e.g., Chan et al., 2004; Hu et al., 2020; Lee et al., 2012, 2015). We also found a very high XCO_2 enhancement (12.2 ppm over a span of around 55 km) in the vicinity of the frontal boundary for this case (Table S2 in Supporting Information S1). To estimate the XCO_2 enhancement around the frontal boundary, we considered warm sector samples obtained between 38.5 and 39.0°N latitude range (i.e., as evinced in the far right corner of panel f) as a reference. Presence of an optically thick low-level cloud band and associated precipitation field around the frontal boundary in central PA (see panels d and b, respectively) resulted in gaps in MFLM measurements. Notwithstanding, we obtained sufficient XCO_2 measurements around the frontal boundary to estimate the XCO_2 enhancement as reported in Table S2 in Supporting Information S1.

For winter cases, two of the seven RFs saw higher values of XCO_2 in the warm sector, with the other five seeing higher XCO_2 in the cold sector than in the warm sector indicating a contrasting feature to summer. The winter MW cases are all from 23 February 2017, from two levels, 3 and 6 km, and are centered around a low-pressure center with the north-south flights crossing the warm front and the east-west flights crossing the cold front. In all these cases, the cold sector MFLM- XCO_2 are higher than the warm sector. The spring has several interesting cases, including observations made on 26 April 2018 and 11 May 2018 (see Supporting Information S1). The 26 April 2018 case potentially sampled two frontal boundaries. Two sharp enhancements are seen in the XCO_2 field and the dewpoint field (see Figure S29 in Supporting Information S1). The additional panel in Figure S29 in Supporting Information S1 illustrate the locations of two frontal boundaries and associated results of XCO_2 spatial variability. For this purpose, we analyzed dewpoint temperature spatial variability obtained along the C-130 track marking the locations of frontal boundaries. The 11 May 2018 case has a sharp enhancement in XCO_2 in the warm sector but was not further investigated due to its location with respect to the remaining warm sector. However, this case provides a clear distinction between the warm and cold sectors with a ΔXCO_2 of 8.5 ppm. Radar measurements confirmed that there were no precipitation events in the northern VA region around the cold front boundary though there were some clouds as appeared in the GOES-16 imagery (Figure S5 in Supporting Information S1). The surface analyses suggested that this was almost a stationary front.

During several RFs, some extraordinary variations in XCO_2 were observed presumably due to prevailing meteorological conditions including location of frontal boundaries and upwind fluxes in the two sectors. The observed XCO_2 fields in both warm and cold sectors were largely affected by the diverse fluxes in the upwind of both sectors while frontal lifting, cloudiness, and ABL depth variability near the frontal boundary contributed to the XCO_2 enhancement frequently observed during the RFs. Two potential factors that become crucial in the MDMs in the XCO_2 fields including XCO_2 frontal contrasts are (a) uncertainties in XCO_2 retrievals in highly variable water vapor environment as mentioned earlier, and (b) atmospheric variability including key meteorological conditions, cloudiness, radiation, horizontal wind, and ABL depths. Nevertheless, some example results reported here strictly confirmed that extraordinary variations in MFLM XCO_2 field (e.g., spatial variability across frontal boundary, enhancement near the frontal boundary, etc.) were similar when compared to in situ CO_2 variability in the ABL from similar environments.

The results reported have important implications for carbon cycle research toward establishing relationship among XCO_2 and ABL- CO_2 fields and surface fluxes and north-south hemispheric gradient in frontal environment which will further guide improved flux estimations and future satellite missions. We note Keppel-Aleks et al. (2011) found that during synoptically active environments, XCO_2 variability is mainly caused by large-scale eddy-driven disturbances of the meridional gradient. Recently, Cui et al. (2021) developed a source-receptor relationship between net ecosystem exchange (NEE) and atmospheric CO_2 variability along flight tracks using the Lagrangian particle dispersion models and confirmed upwind fluxes in frontal sectors mainly drives a major part of the CO_2 frontal contrasts.

5.2. XCO₂ Enhancements

The region of enhanced XCO₂ at the frontal boundary is a complex feature, with several possible explanations for an occurrence. One common feature between all frontal boundary enhancement cases is the presence of extensive cloud cover in the vicinity, or at the region of XCO₂ enhancement. Chan et al. (2004) noted that the cloud cover in the vicinity of a front reduces the photosynthetic uptake of the corn crops in the MW, resulting in CO₂ gradients in frontal regions. This decrease in photosynthetic uptake would lead to an increase in CO₂ near the given region of clouds. This would likely be most prominent in the summer when the photosynthetic uptake is already large. However, based on the region and season, this was also observed in other seasons. We note a comprehensive understanding on the impact of diverse cloud covers near frontal boundaries on photosynthesis uptake and XCO₂ would definitely need further investigation on the time scale of response for flux into atmospheric concentrations. Using a weather-biosphere-online-coupled model, Hu et al. (2021) investigated the development of CO₂ bands in the ABL at the frontal boundary. Similar investigation for XCO₂ enhancement at the frontal boundary using numerical models is a worthwhile topic. Within this work, we documented substantial, new observational findings on XCO₂ spatial variability in frontal environment, and we defined metrics that can be used in future studies including numerical simulations of the transport of GHGs by midlatitude cyclones which is indeed required for accurate inverse CO₂ flux estimation (e.g., Baker et al., 2022).

Using hourly averaged measurements of O₃ from the Air Quality System database, Hegarty et al. (2007) reported that synoptically inactive regimes could lead to the collection of O₃ in a region until a synoptic system transports the pooled O₃ out of the region. Recently, Samaddar et al. (2021) attributed the elevated CO₂ mole fractions along the frontal boundary to continental biogenic CO₂ fluxes. Samaddar et al. (2021) noted that horizontal advection was most dominant near the frontal boundary and positively impacted the amount of CO₂ in the warm sector. While horizontal advection appears to be the main driver in the XCO₂ enhancement near the frontal boundary, the effects of clouds and precipitation need to be analyzed further to fully understand the effects these occurrences have on the variability of the XCO₂ as was performed in Hu et al. (2021). Additionally, because all seven cases of frontal XCO₂ enhancements were associated with the presence of clouds near the frontal boundaries, and four of the seven cases were associated with convection, this is a characteristic feature that warrants future investigations. We used available radar measurements to identify the frontal boundaries associated with presence of strong precipitation bands as shown in Supporting Information S1.

5.3. Comparison Among MFL, GMAO and WRF

The objective behind comparing the MFL-XCO₂ with the WRF-XCO₂ and GMAO-XCO₂ was to identify consistency and quantify differences among the three XCO₂ products in frontal environment. The ΔXCO₂ results obtained from GMAO retrievals were found to agree reasonably well with both sign and magnitudes of MFL observations of ΔXCO₂ for the frontal RFs presented here. Previously, Bell et al. (2020) also found good agreement between GMAO retrieval and MFL observations of XCO₂ spatial variability over the similar region during fair weather RFs of ACT-America in four seasons. Thus, results reported here and in Bell et al. (2020) cumulatively demonstrate the potential of GMAO retrievals of XCO₂ for both frontal and fair weather environments over land. Additionally, an error source not discussed by Campbell et al. (2020) is the potential for biases related to the increased humidity ahead of a frontal boundary, leading to errors in the spectral broadening due to water vapor. Sensitivities of the MFL-XCO₂ retrieval to inputs like meteorology and spectroscopy were studied in some detail in Bell et al. (2020) though only for clear sky conditions. During frontal passages, a large amount of humidity changes occurred, in particular, within warm sector and high contrasts in humidity between the warm and cold sectors while model-simulated water vapor fields were used for MFL retrievals.

For all the MFL measurements presented here, every effort was made to minimize bias due to water vapor. The position of the lasers on the absorption feature were selected to minimize influence from water vapor, but it is not possible to completely eliminate the influence of the continuum. The MFL retrievals use the latest spectroscopy and state-of-the-art reanalysis data, namely MERRA-2, to correct for water vapor. Additionally, the instrument has been calibrated against in situ measurements and was shown to maintain the calibration to within 0.5 ppm over different seasons under different atmospheric conditions, indicating that the residual influence of water vapor bias is small compared to the features being discussed here. The largest biases would be seen where there is large variation of water vapor that is not well captured by the reanalysis products due to the coarser spatial resolution versus the lidar measurement. As spectroscopy and the reanalysis products continue to improve, we

believe that XCO₂ retrieval biases will be further reduced. Eventually, in the future, it will be feasible to combine direct lidar measurements of the water vapor with the CO₂ measurements which would significantly reduce the potential for biases due to water vapor in highly variable cases.

Further research in this direction for those RFs would be very beneficial to examine the biases that might be introduced into MFL by water vapor gradients in frontal environment. For instance, while exploring XCO₂ spatial variability in fair-weather conditions, Bell et al. (2020) investigated the dependence of XCO₂ retrieval on variable water vapor spectroscopy and variable meteorological conditions. It was demonstrated that the MFL retrieval of XCO₂ field is particularly sensitive to water vapor via both the meteorology and spectroscopy. In general, XCO₂ retrieval from MFL measurements strongly depend on water vapor profile which is used to estimate differential optical depth of water vapor (i.e., $\Delta\tau_{\text{H}_2\text{O}}$). For the MFL measurements reported here, we used model-derived (MERRA-2) water vapor profiles. The water vapor absorption cross-sectional profiles were obtained at the model grid points and times based on their meteorological profiles including height, temperature, pressure, and humidity. Additionally, during ACT-America RFs, the MFL used two OFF wavelengths at 50 pm to either side of the ON line (i.e., single CO₂ absorption line centered at 1,571.112 nm, yielding two off lines at 1,571.062 and 1,571.162 nm, referred to as S and L, respectively). Since offline wavelength (L) has higher water vapor sensitivity, we only used the shorter wavelength for calculating differential optical depths (Lin et al., 2020). Previously, Refaat et al. (2015, 2020) though for 2- μm IPDA lidar, and Dobler et al. (2013) and Bell et al. (2020) for MFL, performed a number of sensitivity analyses to determine the impact of water vapor profiles on the XCO₂ retrievals. However, there exist no systematic investigations reporting sensitivity of XCO₂ retrievals on two contrasting water vapor environments as often present in warm and cold sectors of a frontal boundary, and under highly variable water vapor regimes in the boundary layer, in particular, in the warm sector.

Based on the past results reported in Campbell et al. (2020) and Bell et al. (2020), we found it to be plausible that highly variable water vapor regimes along the frontal RF tracks in four seasons would also impact XCO₂ retrievals differently in two contrasting water vapor environments (i.e., warm, and cold sectors), consequently, on ΔXCO_2 . In particular, biases are primarily driven by uncertainty in the true column water vapor versus the reanalysis product column water vapor as interpolated for use in the retrieval as well as any uncertainties in the spectroscopy used. Although we are aware of potential for bias due to uncertainties in water vapor and spectroscopy and have made every effort to minimize that bias using the best in class reanalysis products and latest spectroscopy, it remains an extremely complex task to accurately quantify the bias.

For 26 April 2018, as seen in Figure 7d, WRF-Chem can replicate the frontal contrast by 0.4 ppm difference from the MFL. However, the WRF-XCO₂ was underestimated in warm sector by -3.3 ppm compared to MFL-XCO₂ and the cold sector by -3.7 ppm. A table yielding the key results on frontal contrasts is reported in Supporting Information S1 (see Table S6 in Supporting Information S1). Thus, this case serves as an example of how WRF-Chem simulations can accurately replicate how much the XCO₂ field changed across the boundary but under or overestimated the magnitude of the entire XCO₂ field. The differences in WRF-XCO₂ and GMAO-XCO₂ are likely due in part to the models' data ingested. The GMAO assimilates data from the in situ CO₂ measurements collected during each flight. Notwithstanding, this study identified the MDMs with respect to observational findings on the XCO₂ spatial variability across frontal systems in four seasons.

In general, XCO₂ field in the warm sector for most of the cases was found to be more variable than that in the cold sector, in particular, in summer and winter (see the spread of the box and whiskers in Figures 4a and 4b and results presented in Figures S2c, S6a, S7a, S8a, and S13a in Supporting Information S1). We speculate that higher XCO₂ variability in the warm sector than the cold sector could be attributed to the dominant variability in CO₂ flux in warm sector than in the cold sector. For both spring and fall, such tendencies were not observed (Figures 4c and 4d). Future studies using either observations or model results (or both) of underlying CO₂ fluxes will help demonstrating the differences in CO₂ fluxes across the frontal boundary and their impact on XCO₂ frontal contrasts, if any.

Besides the agreements of XCO₂ variability using MFL observations and model results, we also noted some differences among these products in all four seasons. For some cases, models tend to evince small spread in the box-and-whisker plots (see the boxes in Figure 2, S3, S4, and S5 in Supporting Information S1) while for some other cases we note that simulated XCO₂ yielded larger variability than observations (see, Figures S3, S8, S9, and S16 in Supporting Information S1). As mentioned previously, for the results presented here, the spatial

resolutions in models and observations vary significantly, it will be interesting to examine the impact of different model resolutions on the differences between the observed and simulated XCO₂ variability. In a nutshell, how XCO₂ variability and associated front-relevant metrics are related to model spatial resolution coarseness needs more research, as there are examples of GMAO (with coarser resolution than WRF-Chem) showing larger variability than WRF-Chem as well as MFL observations. Another notable difference was found in the linear regression analyses between Δ XCO₂ from MFL and GMAO and between Δ XCO₂ from MFL and WRF-Chem (Figure 6). In particular, the winter correlation is low (MFL vs. WRF-Chem) and even negative (MFL vs. GMAO) which most likely occurred due to both lower number of samples and poor performance of MFL in winter-2017 campaign due to a known window coating degradation.

Within this work, for the first time, we systematically used the GMAO-XCO₂ fields obtained during multiple frontal RFs in four seasons over land as we introduced a system that establishes calibration standards for OCO-2 and lidar retrievals based on in situ data from the ACT-America campaign. The system assimilates the in situ data into NASA's Goddard Earth Observing System (GEOS) to produce high-resolution, two-dimensional transects of CO₂ along the flight path which we refer to as curtains. Excluding the ability to sample the entire atmosphere at once, any such analysis must make assumptions about the connection of measurements at different places and times to a given retrieval. We chose to use the GEOS general circulation model forced by meteorology from its data assimilation system because their scientific merits are extensively documented. Furthermore, in data-rich environments, the assimilated curtains approach a field constrained by data alone (Bell et al., 2020).

5.4. Frontal Boundary

The frontal flags allowed for obtaining much more precise frontal boundary location rather than estimating the corresponding frontal boundary location with the flight time and location via surface map analysis. We used the flight level frontal flags for most of the analyses. However, when frontal flags were missing along the FT legs (i.e., at the MFL altitudes), we used ABL frontal flags. While these flags have proven to be very useful to this research, there is some uncertainty associated with the frontal flag due to some erroneous measurements of meteorological variables (e.g., water vapor mixing ratio measurements on C-130 platform in summer-2016) or few gaps in measurements across the frontal boundaries during conditions like the presence of thick clouds or a gust front. Because of this uncertainty, for 9 out of the 27 cases, the frontal flag was not available for the given altitude or time of the flight. However, in these cases, the frontal boundary was investigated by analyzing the temperature and dewpoints along the flight track and at the given altitude and estimating the frontal boundary using the location of a significant change in those variables.

Due to the nature of the MFL and the vertical slope of frontal boundaries, identifying the location of the frontal boundary at all altitudes is crucial for identifying the XCO₂ field in each sector. For instance, as illustrated in the conceptual diagram (Figure 1) and exemplified in Figures 2 and 4 (see Supporting Information S1 for other cases), slope of the frontal boundary (in altitude) yielded a northward shift in the frontal boundary in height. However, in the vicinity of the frontal boundary itself, the MFL samples both the warm and cold sectors due to the slanted nature of the frontal boundary. Thus, in those 9 cases where the frontal flag was not used, there may be more uncertainty with what sector is being sampled near the frontal boundary itself. However, the possible error from our frontal boundary estimation appears to be negligible, as Δ XCO₂ were mainly estimated from the 0.5° sectors away from the frontal boundary.

6. Summary, Conclusions, and Outlook

We reported the XCO₂ spatial variability due to the passages of frontal systems in all four seasons using the MFL-retrieved -partial column of XCO₂ measurements below the aircraft. The MFL provides a unique perspective in investigating the varying patterns in XCO₂. For instance, measurements and simulations suggested that XCO₂ field was more heterogeneous in the warm sector compared to the cold sector in all four seasons, as was previously found for ABL-CO₂ fields in frontal sectors (Pal et al., 2020). We also explored how the differences of the three retrievals vary within and among the seasons. Overall, for the first time, we showed how the magnitude and sign of frontal contrasts (i.e., Δ XCO₂) vary by season and illustrated how challenging it is to observe and simulate these frontal differences in presence of significant case-to-case Δ XCO₂ variability.

We demonstrated the ability to use the MFLl to identify the varied structure of XCO₂ across frontal boundaries. Based on the GMAO-XCO₂, we found that the XCO₂ variability in summer (winter) had the most straightforward pattern, with the warm (cold) sector consistently higher than the cold (warm) sector XCO₂. The two transition seasons (fall and spring) did not show a consistent pattern in XCO₂ variability with respect to frontal boundaries. We hypothesized that XCO₂ depends highly on fluxes and significant spatial variability in phenology over land present during these two transition seasons most likely caused the observed XCO₂ frontal contrasts. Despite a lack of a clear pattern in fall, and spring, one clear conclusion is that all of the cases yielded the effect of a frontal passage in the warm sector versus cold sector XCO₂ fields with consistent sign of ΔXCO₂ in all three products.

While comparing the XCO₂ retrievals from MFLl, GMAO and WRF-Chem, and exploring how close those three products were to each other, we found that the MDMs were much smaller compared to the frontal contrasts (i.e., ΔXCO₂) though with some variability among the cases (Figures 6 and 8). Additionally, all three products showed very similar tendency in XCO₂ spatial variability across fronts as confirmed via the linear regression analyses and associated results of high correlation coefficients. Finally, the magnitude and sign of ΔXCO₂ from the three products were found to be very similar in different seasons except WRF-XCO₂ in fall-2017. For instance, for summer-2016, average ΔXCO₂ from MFLl, WRF-Chem and GMAO were found to be 6.4, 5.3, and 4.7 ppm, respectively. All three products showed the presence of an enhanced region of XCO₂ in the vicinity of frontal boundary though with varying magnitudes in different seasons. Cumulatively, the results confirmed that the models can interpret XCO₂ variability across frontal boundaries in all seasons. Our results also illustrated the typical frontal signals in XCO₂ spatial variability in four seasons so that it helps obtain some insights into the fact what satellite-based sensors should be seeing for ΔXCO₂.

Bell et al. (2020) showed the latitudinal gradients in the XCO₂ using OCO-2, MFLl, and GMAO-curtains for some selected days under fair weather conditions. Our analyses provide similar analyses between MFLl-XCO₂ and GMAO-XCO₂ fields but for synoptically active environments. Our work indicates larger MDM of the XCO₂ fields for synoptically active environments compared to fair weather cases. These results provide some information on the ΔXCO₂ that could be expected from OCO-2 measurements. Also, in general, XCO₂ variability in fair weather is of high interests for the OCO-2/3 communities to resolve the issue involved in XCO₂ spatial variability versus instrument noise. In future, we will expand the research to understand better what causes the models' biases and the correlation between the clouds/precipitation and the region of enhanced XCO₂ at the frontal boundary.

Conflict of Interest

The authors declare no conflicts of interest relevant to this study.

Data Availability Statement

The latest version of ACT-America data (both in situ and MFLl observations) is publicly available at the Oak Ridge National Laboratory (ORNL) Distributed Active Archive Center (<https://daac.ornl.gov/actamerica>). The MFLl weighting function and Lite files are available in Lin et al. (2022a, 2022b), respectively on ORNL data archive (<https://doi.org/10.3334/ORNLDAAAC/1891> and <https://doi.org/10.3334/ORNLDAAAC/1892>, respectively). Users need to create an account and can download datasets without any fees. ACT-America airborne and tower GHG observations are also integrated into the NOAA/GML ObsPack data products (Masarie et al., 2014, <https://www.esrl.noaa.gov/gmd/ccgg/obspack/>). A comprehensive description of the datasets is available in Wei et al. (2021). The surface charts were obtained from NOAA's WPC analyses available at https://www.wpc.ncep.noaa.gov/archives/web_pages/sfc/sfc_archive.php.

References

- Baker, D. F., Bell, E., Davis, K. J., Campbell, J. F., Lin, B., & Dobler, J. (2022). A new exponentially decaying error correlation model for assimilating OCO-2 column-average CO₂ data using a length scale computed from airborne lidar measurements. *Geoscientific Model Development*, 15(2), 649–668. <https://doi.org/10.5194/gmd-15-649-2022>
- Barnes, E. A., Parazoo, N., Orbe, C., & Denning, A. S. (2016). Isentropic transport and the seasonal cycle amplitude of CO₂. *Journal of Geophysical Research*, 121(13), 8106–8124. <https://doi.org/10.1002/2016JD025109>
- Bell, E., O'Dell, C. W., Davis, K. J., Campbell, J., Browell, E., Scott Denning, A., et al. (2020). Evaluation of OCO-2 XCO₂ variability at local and synoptic scales using lidar and in situ observations from the ACT-America campaigns. *Journal of Geophysical Research: Atmospheres*, 125(10), e2019JD031400. <https://doi.org/10.1029/2019JD031400>

Acknowledgments

The ACT-America project is a NASA Earth Venture Suborbital 2 project funded by NASA's Earth Science Division (NASA Grant NNX15AG76G), NASA Grant No. 80NSSC19K0730 supported the lead author SW and the co-author SP. Other co-authors were supported by the following NASA grants: NNX15AG76G to Penn State (Davis, Lauvaux); NNL15AQ00B to Exelis (Dobler, Erxleben, McGregor); and NNX15AI97G (O'Dell) to Colorado State University. NASA co-authors were supported by NNH13ZDA001N-EVS2. T. Lauvaux was supported by the French research program CIUDAD. Finally, we thank two anonymous reviewers for their constructive criticisms and helpful suggestions which helped improve both technical and scientific contents of the manuscript.

- Campbell, J. F., Lin, B., Dobler, J., Pal, S., Davis, K., Obland, M. D., et al. (2020). Field evaluation of column CO₂ retrievals from intensity-modulated continuous-wave differential absorption lidar measurements during the ACT-America campaign. *Earth and Space Science*, 7(12), e2019EA000847. <https://doi.org/10.1029/2019ea000847>
- Chan, D., Yuen, C. W., Higuchi, K., Shashkov, A., Liu, J., Chen, J., & Worthy, D. (2004). On the CO₂ exchange between the atmosphere and the biosphere: The role of synoptic and mesoscale processes. *Tellus Series B Chemical and Physical Meteorology*, 56(3), 194–212. <https://doi.org/10.1111/j.1600-0889.2004.00104.x>
- Chevallier, F., Ciais, P., Conway, T. J., Aalto, T., Anderson, B. E., Bousquet, P., et al. (2010). CO₂ surface fluxes at grid point scale estimated from a global 21 year reanalysis of atmospheric measurements. *Journal of Geophysical Research*, 115(21), 1–17. <https://doi.org/10.1029/2010JD013887>
- Chevallier, F., Deutscher, N. M., Conway, T. J., Ciais, P., Ciattaglia, L., Dohe, S., et al. (2011). Global CO₂ fluxes inferred from surface air-sample measurements and from TCCON retrievals of the CO₂ total column. *Geophysical Research Letters*, 38(24), 1–5. <https://doi.org/10.1029/2011GL049899>
- Cui, Y., Zhang, L., Jacobson, A. R., Johnson, M. S., Sanjeev, P., Baker, D., et al. (2021). Seasonal strength of terrestrial net ecosystem CO₂ exchange from North America is underestimated in global inverse modeling. <https://doi.org/10.1002/essoar.10507792.1>
- Davis, K. J., Browell, E. V., Feng, S., Lauvaux, T., Obland, M. D., Pal, S., et al. (2021). The atmospheric carbon and transport (ACT)—America mission. *Bulletin of the American Meteorological Society*, 102(9), 1–54. <https://doi.org/10.1175/bams-d-20-0300.1>
- Davis, K. J., Obland, M. D., Lin, B., Lauvaux, T., O'Dell, C., Meadows, B., et al. (2018). ACT-America: L3 merged in situ atmospheric trace gases and flask data, USA [Dataset]. ORNL DAAC. <https://doi.org/10.3334/ORNLDAAC/1593>
- Dobler, J. T., Harrison, F. W., Browell, E. V., Lin, B., McGregor, D., Kooi, S., et al. (2013). Atmospheric CO₂ column measurements with an airborne intensity-modulated continuous wave 1.57 μm fiber laser lidar. *Applied Optics*, 52(12), 2874–2892. <https://doi.org/10.1364/AO.52.002874>
- Feng, S., Lauvaux, T., Davis, K. J., Keller, K., Zhou, Y., Williams, C., et al. (2019). Seasonal characteristics of model uncertainties from biogenic fluxes, transport, and large-scale boundary inflow in atmospheric CO₂ simulations over North America. *Journal of Geophysical Research: Atmospheres*, 124(24), 14325–14346. <https://doi.org/10.1029/2019JD031165>
- Feng, S., Lauvaux, T., Keller, K., Davis, K. J., Rayner, P., Oda, T., & Gurney, K. R. (2019). A road map for improving the treatment of uncertainties in high-resolution regional carbon flux inverse estimates. *Geophysical Research Letters*, 46(22), 13461–13469. <https://doi.org/10.1029/2019GL082987>
- Gelaro, R., McCarty, W., Suárez, M. J., Todling, R., Molod, A., Takacs, L., et al. (2017). The modern-era retrospective analysis for research and applications, version 2 (MERRA-2). *Journal of Climate*, 30(14), 5419–5454. <https://doi.org/10.1175/JCLI-D-16-0758.1>
- Gerken, T., Feng, S., Keller, K., Lauvaux, T., DiGangi, J. P., Choi, Y., et al. (2021). Examining CO₂ model observation residuals using ACT-America data. *Journal of Geophysical Research: Atmospheres*, 126(18), e2020JD034481. <https://doi.org/10.1029/2020JD034481>
- Gordon, I. E., Rothman, L. S., Hill, C., Kochanov, R. V., Tan, Y., Bernath, P. F., et al. (2017). The HITRAN2016 molecular spectroscopic database. *Journal of Quantitative Spectroscopy and Radiative Transfer*, 203, 3–69. <https://doi.org/10.1016/j.jqsrt.2017.06.038>
- Hegarty, J., Mao, H., & Talbot, R. (2007). Synoptic controls on summertime surface ozone in the northeastern United States. *Journal of Geophysical Research*, 112(14), 1–12. <https://doi.org/10.1029/2006JD008170>
- Hilton, T., Whelan, M., Zumkehr, A., Kulkarni, S., Berry, J. A., Baker, I. T., et al. (2017). Peak growing season gross uptake of carbon in North America is largest in the Midwest USA. *Nature Climate Change*, 7(6), 450–454. <https://doi.org/10.1038/nclimate3272>
- Houze, R. A., Jr., Rutledge, S. A., Matejka, T. J., & Hobbs, P. V. (1981). The mesoscale and microscale structure and organization of clouds and precipitation in midlatitude cyclones. III: Air motions and precipitation growth in a warm-frontal rainband. *Journal of the Atmospheric Sciences*, 38(3), 639–649. [https://doi.org/10.1175/1520-0469\(1981\)038<0639:tmamsa>2.0.co;2](https://doi.org/10.1175/1520-0469(1981)038<0639:tmamsa>2.0.co;2)
- Hu, X.-M., Crowell, S., Wang, Q., Zhang, Y., Davis, K. J., Xue, M., et al. (2020). Dynamical downscaling of CO₂ in 2016 over the contiguous United States using WRF-VPRM, a weather-biosphere-online-coupled model. *Journal of Advances in Modeling Earth Systems*, 12(4), e2019MS001875. <https://doi.org/10.1029/2019MS001875>
- Hu, X.-M., Gourdji, S. M., Davis, K. J., Wang, Q., Zhang, Y., Xue, M., et al. (2021). Implementation of improved parameterization of terrestrial flux in WRF-VPRM improves the simulation of nighttime CO₂ peaks and a daytime CO₂ band ahead of a cold front. *Journal of Geophysical Research: Atmospheres*, 126(10), e2020JD034362. <https://doi.org/10.1029/2020JD034362>
- Humphrey, V., Berg, A., Ciais, P., Gentine, P., Jung, M., Reichstein, M., et al. (2021). Soil moisture–atmosphere feedback dominates land carbon uptake variability. *Nature*, 592(7852), 65–69. <https://doi.org/10.1038/s41586-021-03325-5>
- Hurwitz, M. D., Ricciuto, D. M., Bakwin, P. S., Davis, K. J., Wang, W., Yi, C., & Butler, M. P. (2004). Transport of carbon dioxide in the presence of storm systems over a northern Wisconsin forest. *Journal of the Atmospheric Sciences*, 61(5), 607–618. [https://doi.org/10.1175/1520-0469\(2004\)061<0607:TOCDIT>2.0.CO;2](https://doi.org/10.1175/1520-0469(2004)061<0607:TOCDIT>2.0.CO;2)
- Jacobson, A. R., Fletcher, S. E. M., Gruber, N., Sarmiento, J. L., & Gloor, M. (2007). A joint atmosphere-ocean inversion for surface fluxes of carbon dioxide: 1. Methods and global-scale fluxes. *Global Biogeochemical Cycles*, 21, GB1020. <https://doi.org/10.1029/2006GB002703>
- Jacobson, A. R., Schuldt, K. N., Miller, J. B., Oda, T., Tans, P., Andrews, A., et al. (2020). CarbonTracker CT2019. <https://doi.org/10.25925/39M3-6069>
- Keenan, T. F., & Williams, C. A. (2018). The terrestrial carbon sink. *Annual Review of Environment and Resources*, 43(1), 219–243. <https://doi.org/10.1146/annurev-environ-102017-030204>
- Keppel-Aleks, G., Wennberg, P., Washenfelder, R., Wunch, D., Schneider, T., Toon, G., et al. (2012). The imprint of surface fluxes and transport on variations in total column carbon dioxide. *Biogeosciences*, 9(3), 875–891. <https://doi.org/10.5194/bg-9-875-2012>
- Keppel-Aleks, G., Wennberg, P. O., & Schneider, T. (2011). Sources of variations in total column carbon dioxide. *Atmospheric Chemistry and Physics*, 11(8), 3581–3593. <https://doi.org/10.5194/acp-11-3581-2011>
- Koch, S. E., McQueen, J. T., & Karyampudi, V. M. (1995). A numerical study of the effects of differential cloud cover on cold frontal structure and dynamics. *Journal of the Atmospheric Sciences*, 52(7), 937–964. [https://doi.org/10.1175/1520-0469\(1995\)052<0937:ansote>2.0.co;2](https://doi.org/10.1175/1520-0469(1995)052<0937:ansote>2.0.co;2)
- Lan, X., Tans, P., Sweeney, C., Andrews, A., Jacobson, A., Crotwell, M., et al. (2017). Gradients of column CO₂ across North America from the NOAA global greenhouse gas reference network. *Atmospheric Chemistry and Physics*, 17(24), 15151–15165. <https://doi.org/10.5194/acp-17-15151-2017>
- Lauvaux, T., Schuh, A. E., Uliasz, M., Richardson, S., Miles, N., Andrews, A. E., et al. (2012). Constraining the CO₂ budget of the corn belt: Exploring uncertainties from the assumptions in a mesoscale inverse system. *Atmospheric Chemistry and Physics*, 12(1), 337–354. <https://doi.org/10.5194/acp-12-337-2012>
- Lee, T. R., De Wekker, S. F. J., Andrews, A. E., Kofler, J., & Williams, J. (2012). Carbon dioxide variability during cold front passages and fair weather days at a forested mountaintop site. *Atmospheric Environment*, 46, 405–416. <https://doi.org/10.1016/j.atmosenv.2011.09.068>

- Lee, T. R., de Wekker, S. F. J., Pal, S., Andrews, A. E., & Kofler, J. (2015). Meteorological controls on the diurnal variability of carbon monoxide mixing ratio at a mountaintop monitoring site in the Appalachian Mountains. *Tellus B: Chemical and Physical Meteorology*, 67(1), 25659. <https://doi.org/10.3402/tellusb.v67.25659>
- Lee, T. R., De Wekker, S. F. J., & Pal, S. (2018). The impact of the afternoon planetary boundary-layer height on the diurnal cycle of CO and CO₂ mixing ratios at a low-altitude mountaintop. *Boundary-Layer Meteorology*, 168(1), 81–102. <https://doi.org/10.1007/s10546-018-0343-9>
- Lin, B., Campbell, J. F., Dobler, J., Browell, E. V., Kooi, S. A., Pal, S., et al. (2020). ACT-America: L1 DAOD measurements by airborne CO₂ lidar, eastern USA. [Dataset]. ORNL DAAC. <https://doi.org/10.3334/ORNLDAAC/1817>
- Lin, B., Campbell, J. F., Dobler, J., Browell, E. V., Kooi, S. A., Pal, S., et al. (2022a). ACT-America: L2 remotely sensed column-avg CO₂ by airborne lidar, lite, eastern USA. ORNL DAAC. <https://doi.org/10.3334/ORNLDAAC/1892>
- Lin, B., Campbell, J. F., Dobler, J., Browell, E. V., Kooi, S. A., Pal, S., et al. (2022b). ACT-America: L2 weighting functions for airborne lidar column-avg CO₂, eastern USA. ORNL DAAC. <https://doi.org/10.3334/ORNLDAAC/1891>
- Liu, Y., Wu, C., Liu, L., Gu, C., Black, T. A., Jassal, R. S., et al. (2021). Interannual and spatial variability of net ecosystem production in lForests explained by an integrated physio-logical indicator in summer. *Ecological Indicators*, 129, 107982. <https://doi.org/10.1016/j.ecolind.2021.107982>
- Masarie, K. A., Peters, W., Jacobson, A. R., & Tans, P. P. (2014). ObsPack: A framework for the preparation, delivery, and attribution of atmospheric greenhouse gas measurements. *Earth System Science Data*, 6(2), 375–384. <https://doi.org/10.5194/essd-6-375-2014>
- Miles, N. L., Richardson, S. J., Davis, K. J., Lauvaux, T., Andrews, A. E., West, T. O., et al. (2012). Large amplitude spatial and temporal gradients in atmospheric boundary layer CO₂ mole fractions detected with a tower-based network in the U.S. upper Midwest. *Journal of Geophysical Research*, 117(G1), G01019. <https://doi.org/10.1029/2011JG001781>
- O'Dell, C. W., Connor, B., Bösch, H., O'Brien, D., Frankenberg, C., Castano, R., et al. (2012). The ACOS CO₂ retrieval algorithm-Part 1: Description and validation against synthetic observations. *Atmospheric Measurement Techniques*, 5(1), 99–121. <https://doi.org/10.5194/amt-5-99-2012>
- O'Dell, C. W., Eldering, A., Wennberg, P. O., Crisp, D., Gunson, M. R., Fisher, B., et al. (2018). Improved retrievals of carbon dioxide from Orbiting Carbon Observatory-2 with the version 8 ACOS algorithm. *Atmospheric Measurement Techniques*, 11(12), 6539–6576. <https://doi.org/10.5194/amt-11-6539-2018>
- Pal, S., Behrendt, A., & Wulfmeyer, V. (2010). Elastic-backscatter-lidar-based characterization of the convective boundary layer and investigation of related statistics. *Annales Geophysicae*, 28(3), 825–847. <https://doi.org/10.5194/angeo-28-825-2010>
- Pal, S., & Davis, K. J. (2021). ACT-America campaign Catalog. ORNL DAAC. <https://doi.org/10.3334/ORNLDAAC/1862>
- Pal, S., Davis, K. J., Lauvaux, T., Browell, E. V., Gaudet, B. J., Stauffer, D. R., et al. (2020). Observations of greenhouse gas changes across summer frontal boundaries in the eastern United States. *Journal of Geophysical Research: Atmospheres*, 125(5), e2019JD030526. <https://doi.org/10.1029/2019JD030526>
- Pal, S., Davis, K. J., Pauly, R. M., McGill, M. J., Campbell, L. J., Hoffman, K., et al. (2020). ACT-America: CPL-derived atmospheric boundary layer top height, eastern US, 2016–2018. ORNL DAAC. <https://doi.org/10.3334/ORNLDAAC/1825>
- Pal, S., Lee, T. R., & De Wekker, S. F. J. (2017). A study of the combined impact of boundary layer height and near-surface meteorology to the CO diurnal cycle at a low mountaintop site using simultaneous lidar and in-situ observations. *Atmospheric Environment*, 164, 165–179. <https://doi.org/10.1016/j.atmosenv.2017.05.041>
- Peiro, H., Crowell, S., Schuh, A., Baker, D. F., O'Dell, C., Jacobson, A. R., et al. (2022). Four years of global carbon cycle observed from the Orbiting Carbon Observatory 2 (OCO-2) version 9 and in situ data and comparison to OCO-2 version 7. *Atmospheric Chemistry and Physics*, 22, 1097–1130. <https://doi.org/10.5194/acp-22-1097-2022>
- Peters, G. P., Andrew, R. M., Canadell, J. G., Friedlingstein, P., Jackson, R. B., Korsbakken, J. I., et al. (2020). Carbon dioxide emissions continue to grow amidst slowly emerging climate policies. *Nature Climate Change*, 10(1), 3–6. <https://doi.org/10.1038/s41558-019-0659-6>
- Peters, W., Jacobson, A. R., Sweeney, C., Andrews, A. E., Conway, T. J., Masarie, K., et al. (2007). An atmospheric perspective on North American carbon dioxide exchange: CarbonTracker. *Proceedings of the National Academy of Sciences of the United States of America*, 104(48), 18925–18930. <https://doi.org/10.1073/pnas.0708986104>
- Refaat, T., Petros, M., Singh, U., Antill, C., & Remus, R. (2020). High-precision and high-accuracy column dry-air mixing ratio measurement of carbon dioxide using pulsed 2 μm IPDA Lidar. *IEEE Transactions on Geoscience and Remote Sensing*, 58(8), 5804–5819. <https://doi.org/10.1109/tgrs.2020.2970686>
- Refaat, T. F., Singh, U., Yu, J., Petros, M., Ismail, S., Kavaya, M., & Davis, K. (2015). Evaluation of an airborne triple-pulsed 2 μm IPDA lidar for simultaneous and independent atmospheric water vapor and carbon dioxide measurements. *Applied Optics*, 54(6), 1387–1398. <https://doi.org/10.1364/AO.54.001387>
- Salam, M. A., & Noguchi, T. (2005). Impact of human activities on carbon dioxide (CO₂) emissions: A statistical analysis. *Environmentalist*, 25(1), 19–30. <https://doi.org/10.1007/s10669-005-3093-4>
- Samaddar, A., Feng, S., Lauvaux, T., Barkley, Z. R., Pal, S., & Davis, K. J. (2021). Carbon dioxide distribution, origins, and transport along a frontal boundary during summer in mid-latitudes. *Journal of Geophysical Research: Atmospheres*, 126(9), 1–22. <https://doi.org/10.1029/2020JD033118>
- Schneider, T., Jeevanjee, N., & Socolow, R. (2021). Accelerating progress in climate science Physics Today. *American Institute of Physics*. <https://doi.org/10.1063/PT.3.4772>
- Schuh, A. E., Jacobson, A. R., Basu, S., Weir, B., Baker, D., Bowman, K., et al. (2019). Quantifying the impact of atmospheric transport uncertainty on CO₂ surface flux estimates. *Global Biogeochemical Cycles*, 33(4), 484–500. <https://doi.org/10.1029/2018GB006086>
- Senff, C. J., B'osenberg, J., & Peters, G. (1994). Measurement of water vapor flux profiles in the convective boundary layer with lidar and Radar-RASS. *Journal of Atmospheric and Oceanic Technology*, 11(1), 85–93. [https://doi.org/10.1175/1520-0426\(1994\)011<0085:movf>2.0.co;2](https://doi.org/10.1175/1520-0426(1994)011<0085:movf>2.0.co;2)
- Skamarock, W. C., Klemp, J. B., Dudhia, J., Gill, D. O., Barker, D., Duda, M. G., et al. (2008). A description of the Advanced research WRF version 3 (No. NCAR/TN-475+STR). University Corporation for Atmospheric Research. <https://doi.org/10.5065/D68S4MVH>
- Sweeney, C., Karion, A., Wolter, S., Newberger, T., Guenther, D., Higgs, J. A., et al. (2015). Seasonal climatology of CO₂ across North America from aircraft measurements in the NOAA/ESRL global greenhouse gas reference network. *Journal of Geophysical Research*, 120(10), 5155–5190. <https://doi.org/10.1002/2014JD022591>
- Turner, D. D., Wulfmeyer, V., Berg, L. K., & Schween, J. H. (2014). Water vapor turbulence profiles in stationary continental convective mixed layers. *Journal of Geophysical Research: Atmospheres*, 119(19), 1–15. <https://doi.org/10.1002/2014JD022202>
- Wei, Y., Shrestha, R., Pal, S., Gerken, T., Feng, S., McNelis, J., et al. (2021). Atmospheric carbon and transport—America (ACT-America) datasets: Description, management, and delivery. *Earth and Space Science*, 8(7), e2020EA001634. <https://doi.org/10.1029/2020EA001634>

- Weir, B., Ott, L. E., Collatz, G. J., Kawa, S. R., Poulter, B., Chatterjee, A., et al. (2021). Bias-correcting carbon fluxes derived from land-surface satellite data for retrospective and near-real-time assimilation systems. *Atmospheric Chemistry and Physics*, 21(12), 9609–9628. <https://doi.org/10.5194/acp-21-9609-2021>
- WPC. (2022). NOAA/national weather Service, national Centers for environmental prediction, weather prediction Center [dataset]. stl. Retrieved from https://www.wpc.ncep.noaa.gov/archives/web_pages/sfc/sfc_archive.php
- Wulfmeyer, V., Pal, S., Turner, D. D., & Wagner, E. (2010). Can water vapour Raman lidar resolve profiles of turbulent variables in the convective boundary layer? *Boundary-Layer Meteorology*, 136(2), 253–284. <https://doi.org/10.1007/s10546-010-9494-z>
- Wunch, D., Toon, G. C., Blavier, J. F. L., Washenfelder, R. A., Notholt, J., Connor, B. J., et al. (2011). The total carbon column observing network. *Philosophical Transactions of the Royal Society A: Mathematical, Physical & Engineering Sciences*, 369(1943), 2087–2112. <https://doi.org/10.1098/rsta.2010.0240>
- Wunch, D., Wennberg, P. O., Osterman, G., Fisher, B., Naylor, B., Roehl, C. M., et al. (2017). Comparisons of the orbiting carbon observatory-2 (OCO-2) XCO₂ measurements with TCCON. *Atmospheric Measurement Techniques*, 10(6), 2209–2238. <https://doi.org/10.5194/amt-10-2209-2017>
- Zhang, L., Davis, K. J., Schuh, A. E., Jacobson, A. R., Pal, S., Cui, Y. Y., et al. (2022). Multi-season evaluation of CO₂ weather in OCO-2 MIP models. *Journal of Geophysical Research: Atmospheres*, 127(2), e2021JD035457. <https://doi.org/10.1029/2021JD035457>